



This is a repository copy of *On the modelling of precipitation kinetics in a Turbine disc nickel based superalloy*.

White Rose Research Online URL for this paper:  
<https://eprints.whiterose.ac.uk/159428/>

Version: Accepted Version

---

**Article:**

Anderson, M.J. [orcid.org/0000-0001-5552-4459](https://orcid.org/0000-0001-5552-4459), Schulz, F., Lu, Y. et al. (4 more authors) (2020) On the modelling of precipitation kinetics in a Turbine disc nickel based superalloy. *Acta Materialia*, 191. pp. 81-100. ISSN 1359-6454

<https://doi.org/10.1016/j.actamat.2020.03.058>

---

Article available under the terms of the CC-BY-NC-ND licence  
(<https://creativecommons.org/licenses/by-nc-nd/4.0/>).

**Reuse**

This article is distributed under the terms of the Creative Commons Attribution-NonCommercial-NoDerivs (CC BY-NC-ND) licence. This licence only allows you to download this work and share it with others as long as you credit the authors, but you can't change the article in any way or use it commercially. More information and the full terms of the licence here: <https://creativecommons.org/licenses/>

**Takedown**

If you consider content in White Rose Research Online to be in breach of UK law, please notify us by emailing [eprints@whiterose.ac.uk](mailto:eprints@whiterose.ac.uk) including the URL of the record and the reason for the withdrawal request.



[eprints@whiterose.ac.uk](mailto:eprints@whiterose.ac.uk)  
<https://eprints.whiterose.ac.uk/>

# On the modelling of precipitation kinetics in a Turbine disc nickel based superalloy.

M. J. Anderson<sup>a</sup>, F. Schulz<sup>b</sup>, Y. Lu<sup>b</sup>, H. S. Kitaguchi<sup>b</sup>, P. Bowen<sup>b</sup>, C. Argyraklis<sup>c</sup>, H. C. Basoalto<sup>a</sup>

<sup>a</sup>*Department of Materials Science & Engineering, The University of Sheffield, Mappin Street, Sheffield S1 3JD, UK*

<sup>b</sup>*School of Metallurgy and Materials, University of Birmingham, Edgbaston, Birmingham B15 2TT, UK*

<sup>c</sup>*Rolls-Royce plc, Derby, DE24 8BJ, UK*

---

## Abstract

The precipitation kinetics of gamma prime in the nickel based superalloy RR1000 has been characterised after solid-solution heat treatments and isothermal aging conditions relevant to service conditions. Multi-modal precipitate dispersions are formed within the alloy. Numerical methods are presented for determining the three dimensional size of the particle populations combining information obtained from Scanning Electron microscopy and Transmission Electron microscopy. This information has been used to develop a multi-component mean-field model descriptive of precipitation kinetics. The smallest particle population increases in mean size during isothermal aging at 700°C where classical mean-field models of coarsening kinetics suggest that these particles should dissolve. A phenomenological model has been proposed to capture this behaviour within a statistical formulation that is applicable to both processing and service conditions.

*Keywords:* Nickel based superalloy, RR1000, particle coarsening, mean-field theory, multi-components systems, multi-modal particle radius distribution

---

## 1. Introduction

Critical components within turbine engines are often manufactured from nickel based superalloys due to their ability to retain their mechanical prop-

erties at elevated temperature. The polycrystalline powder metallurgy nickel based superalloy RR1000 is used for turbine disc applications. This alloy is precipitate strengthened through the presence of the  $\gamma'$  phase and is carefully heat treated to obtain a multi-modal particle dispersion in the as-heat treated condition. By heat treating RR1000 above or below the  $\gamma'$  solvus temperature it is possible to obtain coarse-grain or fine-grain microstructures that provide different mechanical properties. A sub-solvus solid solution heat treatment retains  $\gamma'$ , which grow to radii varying between 0.5-1.5 $\mu\text{m}$ . These precipitates impede grain-growth, maintaining the grain size achieved after forging of the component during solid-solution treatment. The populations of  $\gamma'$  which precipitate during cooling after the solid solution treatment and continue to grow and coarsen during aging are referred to as secondary and tertiary particles. The first population of particles to precipitate are referred to as secondary particles, with the following particle populations described as tertiary precipitates. In the heat-treated condition, secondary particles have sizes varying between 50-500nm, whilst tertiary particles refer to the smaller precipitates observed in the material.

A super-solvus heat treatment dissolves all  $\gamma'$  during solid solution heat treatment. The grains grow until they are restricted by any carbides present.

Mechanical properties such as yield, creep, and fatigue behaviour are sensitive to the size, volume fraction and spatial arrangement of these  $\gamma'$  particle populations. The ability to model the kinetics of these precipitates is important, and is needed to assist in the design of heat treatments and to capture the stability of the microstructure during component service. Information regarding the size and volume fraction of these precipitates can be used in physical based descriptions of plasticity.

Experiments have been performed to measure the  $\gamma'$  dispersions after different solid solution treatments, and determine precipitation coarsening kinetics during conditions relevant to service. Multi-modal  $\gamma'$  particle distributions have been characterised using a combination of Scanning Electron Microscopy (SEM) and Transmission Electron Microscopy (TEM). The micrographs provide differ-

ent information regarding the size of the precipitates, with SEM micrographs showing the particles revealed in a 2D cross section through the material, and TEM showing the outline of the 3D particle morphology captured within the TEM sample. A framework is presented which allows for the merging of experimental data gained from either method for comparison with mean-field predictions. The precipitate dispersions have been characterised from specimen that have undergone SSTs at sub and super-solvus temperatures, followed by either an air cooling or furnace cooling. The results indicate that for RR1000, the tertiary  $\gamma'$  precipitates nucleate during the quench after solid solution treatment and not during the subsequent aging heat treatment. The isothermal aging kinetics of the secondary and tertiary precipitates within the coarse-grain variant of RR1000 has been measured at temperatures of 700°C, 750°C, and 800°C after aging times of 50h, 100h, and 500h. The results show that the tertiary particles have coarsened and are still present the material after exposure to isothermal aging for 500h at 700°C, however the tertiary precipitate volume fractions reduce significantly when exposed for similar times at 750°C. The tertiary precipitates have fully dissolved after 500h at 800°C.

The driving force behind the formation, growth and coarsening of the different populations of  $\gamma'$  is the reduction in free energy of the system [1]. Ostwald ripening kinetics describes the coarsening of particles driven by the reduction of the interfacial energy. The difference in molar volume between the  $\gamma'$  and  $\gamma$  phases results in a distortion of the lattice. This misfit strain affects growth behaviour and influences particle morphology [2, 3]. Particle size and morphology are also impacted by coalescence events. The composition of the different populations of particles present in as-quenched RR1000 have been measured to differ significantly [4]. The local precipitate and matrix chemistries would change the chemical driving force for phase transformation for the different populations of precipitates. The differences in composition might also impact the molar volume, and thus the elastic misfit, further complicating precipitate kinetics.

A mean-field modelling approach has been adopted to simulate precipitation kinetics, where the particle morphology is approximated by spheres and

the growth rate is assumed to be a function of the size of the particle, and composition. The particle growth rate may be derived by equating the solute needed to grow a particle by an increment  $dR$  to the amount of solute that can diffuse toward the particle - matrix interface within a time increment  $dt$  [5, 6, 7, 8, 9]. Such approaches which resolve the composition and fluxes at the particle-matrix interface may be referred to as a “local equilibrium” approximation. Svoboda *et al.* [10] have developed an alternative approach applying the thermodynamic extremum principle (TEP) to derive the particle growth rate and chemical driving force for precipitate phase transformations. One advantage of the Svoboda *et al.*’s model is that it does not require the resolution of the composition at the precipitate interface, accounting for the Gibbs-Thomson effect, which is not trivial when considering a multi-component alloy.

It is convenient to consider particle kinetics in terms of the following distinct regimes:

- (i) The regime of particle nucleation and growth: where the matrix is super-saturated with precipitate forming solute species.
- (ii) The regime of coarsening: where the particle volume fraction approaches equilibrium and there is conservation of solute within the precipitate phase.
- (iii) The regime of dissolution: where the critical particle radius exceeds the largest particle within the ensemble, and occurs when the volume fraction of particles is higher than equilibrium.

Gabb *et al.* [11] applied different growth rates to the precipitates in regimes of (i) nucleation and growth, and (ii) coarsening. The difference in kinetics is caused by the large matrix super-saturation that develop during nucleation and growth, accelerating precipitation kinetics. Chen *et al.* [8] included the diffusion distance when calculating the diffusive fluxes surrounding precipitates, accounting for this behaviour. This detail is lacking in other model formulations, such as those by Jou *et al.* [12], and Svoboda *et al.* [10].

In previous work, the particle growth rate derived by Svoboda *et al.*’s [10]

was applied to simulate the coarsening behaviour of a bimodal distribution of precipitates towards a unimodal dispersion in the Ni-based superalloy IN738LC [13]. The model was then further developed to simulate precipitation kinetics in both Inconel 718 [14] and Inconel 625 [15]. In this work, Svoboda *et al.*'s [10] particle growth rate has been adapted to include changes in the diffusion distance of the fluxes during regimes of growth to simulate the accelerated growth kinetics during the quench from a solid solution treatment. The modification is useful in accelerating growth kinetics, however does not fundamentally change predicted behaviour.

When applying Svoboda *et al.*'s [10] particle growth rate to simulate the coarsening of the secondary and tertiary precipitates in the coarse-grain variant of RR1000, the tertiary precipitates are predicted to dissolve however experimental data show that they increase in mean radius. The ability to correctly predict the coarsening behaviour of tertiary particles is vital when simulating creep in nickel based superalloys. Semiatin *et al* [16] have developed a “local-field” approximation of the concentration gradients that develop between secondary particles during a quench from a solid-solution treatment, improving the description of the nucleation and growth kinetics of tertiary precipitates. The model does not yet account for the homogenization of these concentration fields, which may occur during a slow cool after a solid solution treatment, during aging, and in service.

This work provides an alternative approach to capturing tertiary kinetics. The hypothesis is that only a fraction of tertiary particles directly competes with secondary precipitates, whilst the remaining tertiary particle population compete amongst themselves, allowing for the isolated tertiary particles to coarsen rather than dissolve. Many mean-field formulations of precipitation derive particle growth rates that can be manipulated into a form that reveals a critical particle radius [5, 6, 7, 8, 9, 10], where particles larger than this value grow, and those smaller shrink. Such models apply the critical particle radius to all precipitates within the dispersion, and assume that the neighbourhood of all particles are the same. This is not true for the tertiary precipitates, which form

in regions of high super-saturation, far from the secondary particles. In addition, depletion zones develop surrounding the secondary particles [17, 18], separating the particle populations, reducing the growth rate of the secondary particles, and increasing differences in chemistry considering the two particle populations. It is proposed that the unexpected growth of the tertiary particles is due to the time needed for the depletion zones to homogenize, and for secondary particles to come into direct competition with tertiary particles. An Avrami parameter is used to describe the fraction of tertiary particles which are isolated from the secondary particle population and capture how the fraction diminishes through diffusion. Different growth rates are applied to the isolated tertiaries compared to the tertiaries which compete directly with secondary particles.

The advantage of this approach is that through the simplifying assumptions regarding the solute concentration field and particle morphology, computation speed is considerably faster than morphologically explicit descriptions of microstructural evolution [19, 20]. Another benefit is the ability to capture the kinetics of a statistically representative number of particles which can prove challenging when considering the changes in particle concentration that occur during typical heat treatments applied to nickel based superalloys. The limitations of the model arise due to the treatment of precipitate interactions, the precipitate morphology, and local variations in composition. Despite these issues, the model is capable of capturing the evolution of the mean size of the different populations of particles with reasonable accuracy.

The following section presents the experimental methods and the characterisation of the  $\gamma'$  dispersions in different heat treated conditions.

Section 3 presents the mean-field model detailing how the treatment of the isolated tertiary precipitates, followed by a Section outlining the numerical implementation. Section 5 presents the model predictions considering sub-solvus and super-solvus SST, in addition to isothermal aging. Sections 6 and 7 discuss and conclude the paper.

## 2. Experimental

### 2.1. Metallurgical methods

Two variants of the nickel based superalloy RR1000 were used in this study; fine-grain RR1000 in the as-forged condition and coarse-grain RR1000 in the as-heat treated condition.

The coarse-grain variant is obtained by applying a solid solution treatment consisting of a 2h aging at 1170°C followed by 16h at 760°C to the as-forged condition. The nominal composition of RR1000 is given in Table 1. The as-forged coupons were used to examine sub-solvus and super-solvus heat treatments, followed by either an air-quench or furnace-quench. The coarse-grained material was used to study the aging kinetics of the tertiary and secondary particle populations. This involved isothermal aging at temperatures of 700°C, 750°C and 800°C for time intervals of 50 hours, 100 hours and 500 hours.

Scanning Electron Microscopy (SEM) and Transmission Electron Microscopy (TEM) have been used to obtain micrographs to quantify the distribution in size and volume \area fraction of the particle dispersions. TEM has been necessary to measure small tertiary particles with greater accuracy. The measurements of tertiary particles using SEM is limited by error introduced by etching and poor resolution of such small particles.

The SEM specimens have been prepared using conventional metallographic preparation, using an electrochemical etch to remove the  $\gamma$  and reveal the  $\gamma'$  particles [21]. This involves mounting each specimen in Bakelite, and then applying a sequence of abrasive and polishing steps to obtain a surface suitable for micrography. In order to reveal  $\gamma'$  particles, the specimens were electrochemically etched using a 10% orthophosphoric acid solution in water. A voltage of 2.5  $V_{dc}$  was applied for 1-2 seconds to obtain a shallow etch, appropriate for the current image analysis. Backscatter and secondary electron images were taken using a Jeol JSM-7000F SEM.

TEM samples were obtained by taking thin slices of approximately 0.3 mm in thickness from the samples using electro-discharge machining. Discs of 3 mm

Table 1: Nominal composition of RR1000 (at.%)

Al	B	C	Co	Cr	Hf	Mo	Ni	Ta	Ti	Zr
6.35	0.08	0.13	17.94	16.49	0.16	2.98	balance	0.63	4.29	0.04

diameter were punched from these slices and manually ground to 80 - 100  $\mu\text{m}$  thickness. The foils were prepared by twin-jet electro-polishing using a Struers TenuPol-3. The polishing chemical used consisted of 10 vol.% of Perchloric acid with 90 vol.% of ethanol. The polishing was performed at  $-25^{\circ}\text{C}$ , at 20V and 0.5A until a hole appeared.

## 2.2. Characterisation of the $\gamma'$ dispersions

Quantitative image analysis has been performed to measure particle radius distributions, area fractions and volume fractions. The SEM and TEM micrographs have been processed following the standard imaging techniques described by Payton *et al.* [21] using either ImageJ [22] or the MATLAB Image Processing Toolbox [23]. Approximations of the area fraction of particles from SEM images can have errors as high as  $\pm 5\%$ .

The SEM and TEM micrographs show different information regarding the  $\gamma'$  dispersion. The SEM images show a cross section of the microstructure, whilst the TEM images provide an elevation view of the 3D microstructure. Stereological methods exist to approximate the 3D particle radius from 2D information obtained from SEM micrographs. Empirical relationships can be used to approximate the mean 3D particle radius from the mean 2D particle radius [24]. If the 2D particle size distribution has been characterised with sufficient detail, numerical approximations may be applied to approximate the 3D dispersion from 2D measurements [25]. Figure 1 illustrates what would be observed in an SEM when examining a system of spherical non-penetrating particles. The etching process complicates what is observed in the SEM in a number of ways; (i) the particles which are mainly embedded in the sample are further exposed as the surrounding matrix is removed, (ii) the particles which are mainly cut away during grinding and polishing may be removed completely as the supporting

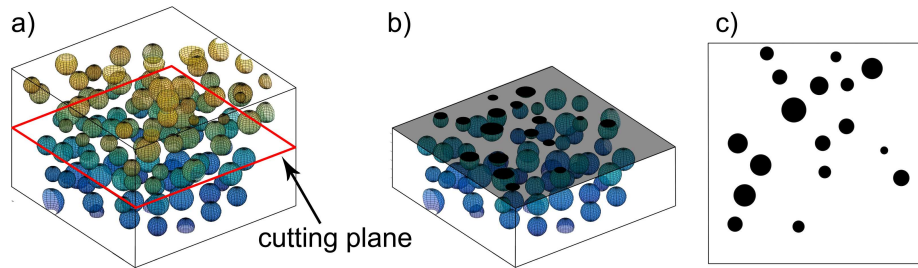


Figure 1: (a) A 3D particle system containing spherical non-penetrating particles, and a cutting plane where the sample has been ground during metallurgical processing. (b) The cross section of particles created after cutting, grinding, polishing and etching of the sample. (c) An illustration of the particles that would appear on the SEM.

matrix is etched away, and (iii) the etching of the matrix may reveal additional particles present just beneath the surface. As a result, the particle distribution observed in an SEM micrograph of an etched microstructure appears different to what would be expected when considering the cross sections of spherical particles created from a planar cut through the dispersion. This is illustrated in Figure 2 which considers the impact of etching upon the resulting 2D particle radius distribution (PRD). The distributions are calculated numerically by generating random ensembles of 3D particle dispersions and examining the particles found on a plane cutting through the volume. The thickness of the cut is increased, simulating the etching process with some particles being removed and others appearing larger. As the amount of matrix removed is increased, the observed distribution changes shape. Another consideration is that SEM cannot accurately capture particles below a certain limit, which is why TEM is needed for characterising small particle populations.

Figure 3 illustrates what is observed in a TEM sample, where Figure 3 (a) shows the three dimensional particle system of non-penetrating spherical particles contained within a portion of the TEM sample. Figure (b) illustrates the view observed from the TEM, looking through the sample.

PRD functions are used to characterise the particle dispersions. Let the size of the precipitates be defined by the radius of a circle or sphere of equivalent

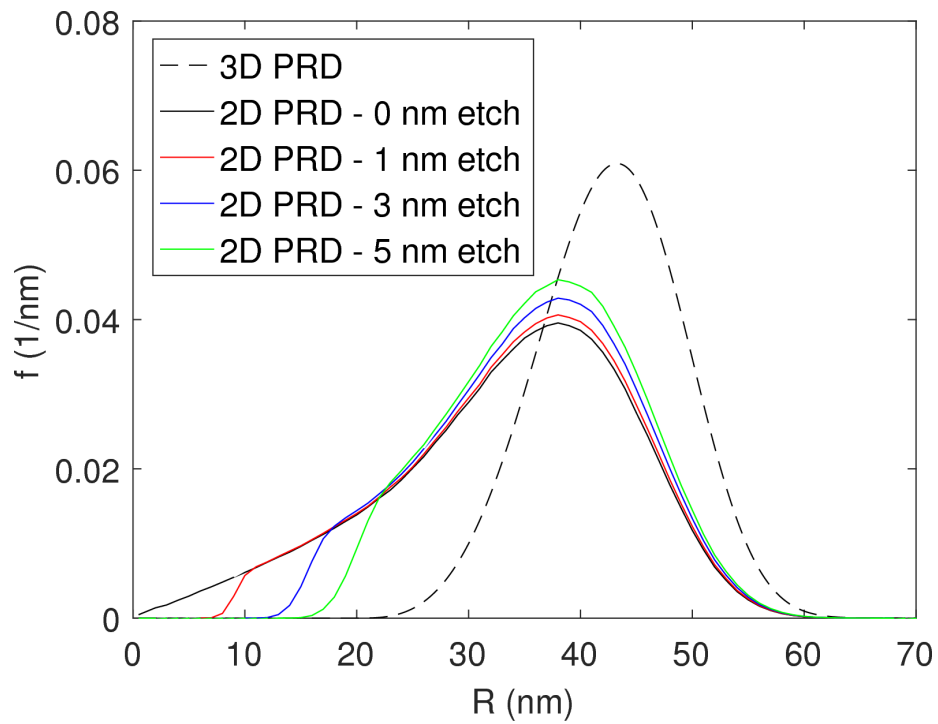


Figure 2: The impact of etching upon the observed particle radius distribution (PRD) from a cross section of the microstructure.

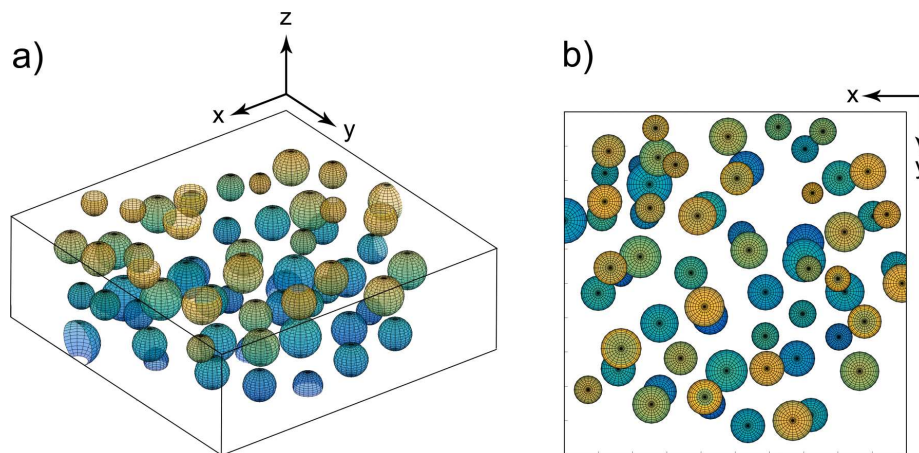


Figure 3: (a) A 3D particle system containing spherical non-penetrating particles where the height of the 3D domain is similar to the thickness of the TEM specimen (b) The view observed when examining such a particle dispersion using a TEM.

area or volume depending on whether we are considering a cross section of the particle or the 3D size of the particle. Histograms have been generated from the measured particle equivalent radii from SEM and TEM micrographs. Different distribution functions are needed to describe the information obtained from SEM and TEM. Let  $\mathcal{F}_{2D}(r)dr$  describe the number of particles with a radius varying within the closed interval of  $[r, r + dr]$  found within a unit area. Similarly,  $\mathcal{F}_{3D}(R)dR$  describe the number density of particles found within a unit volume considering particles with a radius within the closed interval of  $[R, R + dR]$ . The area fraction and volume fraction of spherical particles are equivalent, and are calculated as follows

$$\begin{aligned}\phi_{2D} &= \pi \int_0^{\infty} r^2 \mathcal{F}_{2D}(r) dr \\ \phi_{3D} &= \frac{4\pi}{3} \int_0^{\infty} R^3 \mathcal{F}_{3D}(R) dR\end{aligned}\tag{1}$$

where  $\phi_{2D}$  and  $\phi_{3D}$  describe the area fraction and volume fraction, respectively.

The functions  $f_{2D}(r)dr$  and  $f_{3D}(R)dR$  are the probability density functions associated with  $\mathcal{F}_{2D}(r)dr$  and  $\mathcal{F}_{3D}(R)dR$ . Let  $\mathcal{H}_{2D}(r)$  describe the histogram obtained from particle radii from an SEM micrograph. The radius probability functions  $f_{2D}(r)dr$  is obtained from the histogram as shown below

$$f_{2D}(r) = \mathcal{H}_{2D}(r) \left[ \int_0^{\infty} \mathcal{H}_{2D}(r') dr' \right]^{-1}\tag{2}$$

Similarly

$$f_{3D}(R) = \mathcal{H}_{3D}(R) \left[ \int_0^{\infty} \mathcal{H}_{3D}(R') dR' \right]^{-1}\tag{3}$$

If the volume fraction or area fraction of particles is known, the radius probability functions can be corrected to determine  $\mathcal{F}_{2D}(r)dr$  and  $\mathcal{F}_{3D}(R)dR$ . For example

$$\mathcal{F}_{2D}(r) = \phi_{2D} f_{2D}(r) \left[ \pi \int_0^{\infty} f_{2D}(r') [r']^2 dr' \right]^{-1}\tag{4}$$

and to convert  $f_{3D}$  to  $\mathcal{F}_{3D}$

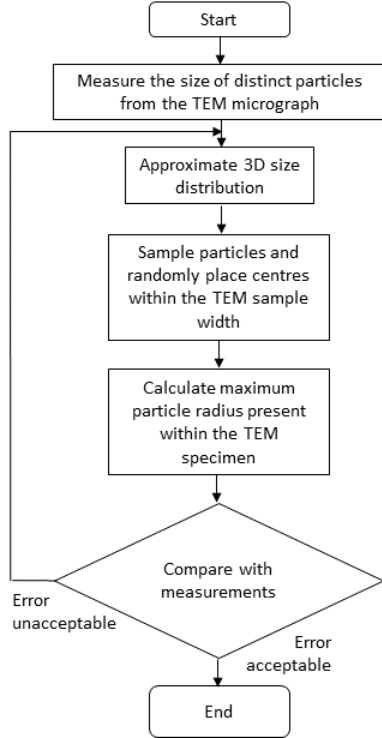
$$\mathcal{F}_{3D}(R) = \phi_{3D} f_{3D}(R) \left[ \frac{4\pi}{3} \int_0^{\infty} f_{3D}(R') [R']^3 dR' \right]^{-1}\tag{5}$$

The particle area fraction can be measured from quantitative image analysis of SEM micrographs with some error. The error may arise from defects introduced during metallurgical preparation, over or under etching, the resolution and quality of the micrograph, and the ability to accurately detect the edges of the precipitate.

A method has been developed to approximate the size and volume fraction of particles from conventional TEM micrographs. The approach aims to reconstruct the 3D microstructure utilising the information available from the TEM image and builds upon the framework developed by Sonderegger [26]. Sonderegger [26] used numerically generated particle dispersions to verify the calculations of the particle size and volume fraction. In the method developed in this work, numerically generated particle dispersions are used to iteratively approximate the particle dispersion, comparing features directly with the TEM micrographs. The thickness of the TEM specimen must be known and can be calculated using the convergent-beam-electron-diffraction method [27]. As illustrated in Figure 3, the TEM micrographs shows overlapping particles within a 3D volume. Some of the particles are partially within the volume, as they have been cut when creating the TEM specimen.

To obtain the information needed for this method, the TEM micrographs are processed twice. The first step is to determine the 3D size of the particles from the micrograph, and is described in Figure 4a). Individual particles are identified and measured in the image, creating a distribution of particle radii. These measurements are not the true 3D size of the particles, as some particles may not be totally present within the TEM specimen. By knowing the TEM foil thickness, the 3D size can be approximated, using the associated particle radius accumulative probability to generate particles numerically, and randomly placing them within the thickness of the TEM specimen. The largest radius of the particle within the TEM volume is then calculated, creating a distribution of cut particles that can be compared to the data obtained from the TEM micrograph. An example of the results are illustrated in Figure 5. The approximated 3D particle size can be adjusted until the experimental data is captured

a) Approximation of  $f_{3D}(R)$



b) Approximation of  $\phi$

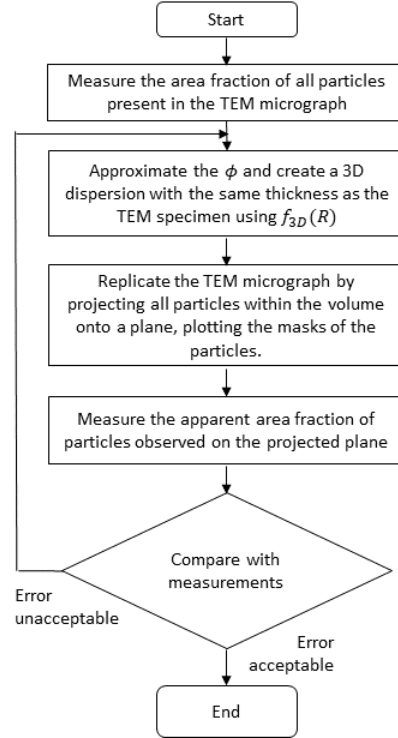


Figure 4: a) A flowchart describing the steps taken to approximate the 3D size of particles from TEM micrographs. b) A flowchart describing the steps taken to approximate the volume fraction of particles from TEM micrographs.

adequately.

The purpose of the second step is to determine the volume fraction of particles, and is described in Figure4b). Using the previously calculated 3D size distribution of particles, three dimensional particle dispersions are then generated numerically with different volume fractions of particles. The size of the volume created is made such that the thickness is the same as the TEM specimen thickness. The mask of the generated particles are then projected onto an elevation view, recreating what is observed in the TEM micrograph. The area fraction of the projection is then compared with the area fraction measured from image processing of the TEM micrograph. An iterative process is then used to

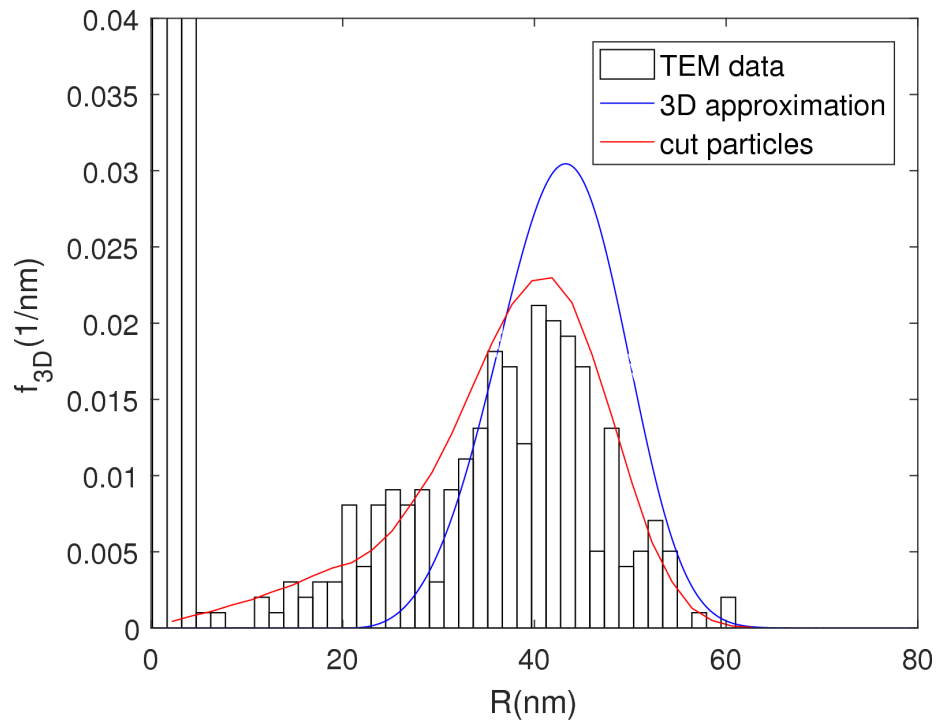


Figure 5: The approximated 3D PRD of the secondary particle population and the distribution of maximum particle radii totally within the TEM thickness. This is compared with experimental data measured from TEM micrographs.

determine the volume fraction of particles that best reproduces the measured area fraction. Error is incurred as the thickness of the TEM specimen is not uniform. This error can be quantified by repeating the analysis for the upper and lower approximations of the sample thickness.

The information obtained from the TEM and SEM analysis can be displayed together by either approximating the 3D particle size distribution of particles observed in SEM images, or by calculating the 2D cross sectional data from the TEM measurements.

The 3D→2D conversion can be calculated analytically as follows [28],

$$f_{2D}(r) = \frac{1}{M_c} \int_0^\infty \frac{f_{3D}(R)}{R\sqrt{R^2 - r^2}} dR \quad (6)$$

where  $r$  is the radius of the 2D cross section of interest, and  $R$  is the 3D radius of the particles.  $M_c$  is a constant used to ensure unity of the zeroth moment of the  $f_{2D}$  function. Alternatively, the  $f_{2D}(r)$  may be calculated numerically [25].

It is difficult to view multi-modal particle radius distribution functions using either the  $\mathcal{F}_{2D}(r)$  or  $\mathcal{F}_{3D}(R)$  distribution functions. The number density concentrations of  $\mathcal{F}_{3D}(R)$  for the different particle populations can vary by orders of magnitude, making it necessary to apply a logarithm to the y-axis to view all particle populations. Alternatively, the distributions can be displayed in the area/volume fraction reformulation using the  $G_{2D}(r)$  and  $G_{3D}(R)$  functions, respectively. They are calculated as shown below

$$G_{2D}(r) = \pi r^2 \mathcal{F}_{2D}(r) \quad (7)$$

$$G_{3D}(R) = \frac{4\pi}{3} R^3 \mathcal{F}_{3D}(R) \quad (8)$$

### 2.3. Solid solution treatment

Test specimens have been cut from a forged disc of RR1000, provided by Rolls-Royce plc. The coupons have been subject to solid solution heat treatments (SST) at temperatures of either 1120°C or 1160°C for 2 hours, followed

by an air-cool or a furnace cool. The temperature of the specimens were monitored using N-type thermocouples, which were inserted into 1mm deep holes, and secured using thermal cement. The thermal history applied to the specimens is presented in Figure 6. Figure 7 presents the as-forged microstructure and the particle dispersions obtained after an air cool and furnace cool from a sub-solvus solid solution treatment. Figure 8 shows representative micrographs taken of specimens after a super-solvus SST followed by an air quench or furnace quench.

The measurements from the SEM and TEM data are summarised in Table 2. The slower cooling rates considering both sub-solvus and super-solvus conditions result in larger secondary and tertiary precipitates. The sub-solvus furnace cooled secondary precipitates are roughly half the size of the furnace cooled super-solvus specimen. The area fraction of primary particles in the sub-solvus furnace cooled specimen has increased compared to the sub-solvus air cool condition, indicating that the primary particles have grown during the furnace cool. The area fraction of secondary particles is greater in the air-cooled conditions compared to the furnace cooled conditions for both sub and super-solvus SST heat treatments. The size of the tertiary precipitates is greater in the furnace cooled conditions compared to the air-cooled conditions however the trend in volume fractions differs. For the sub-solvus SST condition, an air-cool results in a higher volume fraction of tertiary precipitates. For super-solvus conditions, this trend is reversed with the furnace cooled condition having a higher volume fraction of tertiary  $\gamma'$ .

#### *2.4. Isothermal aging*

Isothermal aging has been performed on specimens of as-heat treated coarse-grain RR1000. SEM images of the initial microstructure is shown in Figure 9. Figures 10 and 11 present the micrographs taken of the aged specimens for different times and temperatures focusing on the secondary and tertiary particles, respectively.

Statistical measurements of the secondary and tertiary particle dispersions

Table 2: Summary of measured particle dispersions in SST specimens. This includes the as-received forged condition, and solid solution treated (SST) specimens heat treated above and below the  $\gamma'$  solvus temperature for 2h, followed by either an air cool (AC) or furnace cool (FC)

Condition	Primary		Secondary		Tertiary	
	$\phi_{2D}$	$\langle R_{2D} \rangle$	$\phi_{3D}$	$\langle R_{3D} \rangle$	$\phi_{3D}$	$\langle R_{3D} \rangle$
	(%)	(nm)	(%)	(nm)	(%)	(nm)
As-forged	25	524	16.0	44.6	1.4	5.5
1120°C SST + AC	9	608	34.1	39.6	1.9	4.0
1120°C SST + FC	14.5	502	30.5	65.6	0.5	7.6
1160°C SST + AC	0	0	44.9	44	0.2	8.5
1160°C SST + FC	0	0	41.3	112	3.0	22.4

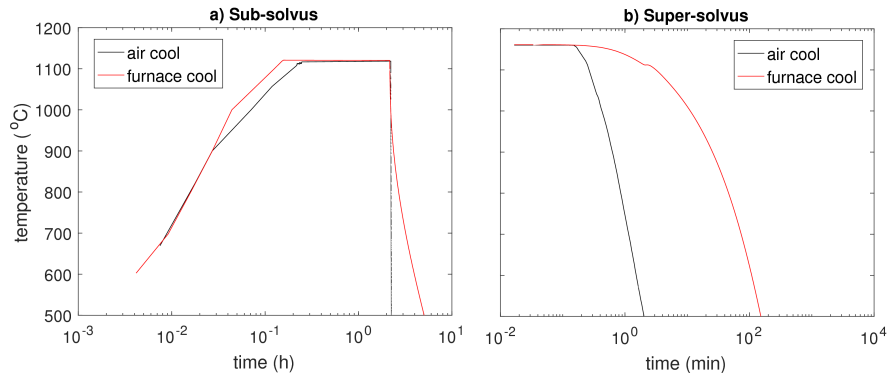
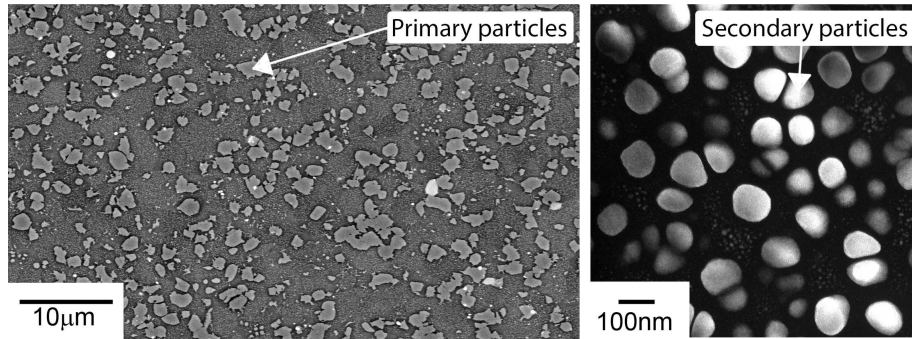
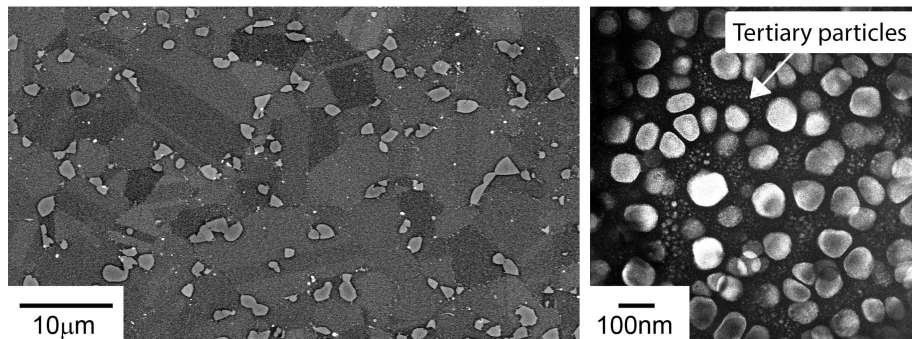


Figure 6: The thermal history of the a) sub-solvus heat treatments and b) the super-solvus heat treatments.

**(a) As-forged**



**(b) Sub-solvus SST and air cool**



**(c) Sub-solvus SST and furnace cool**

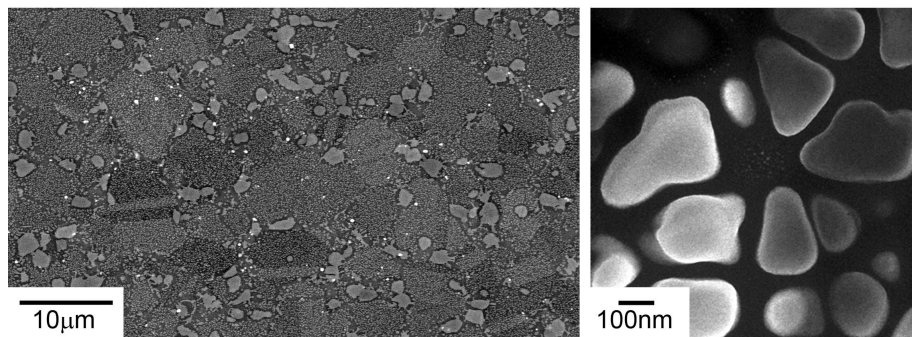
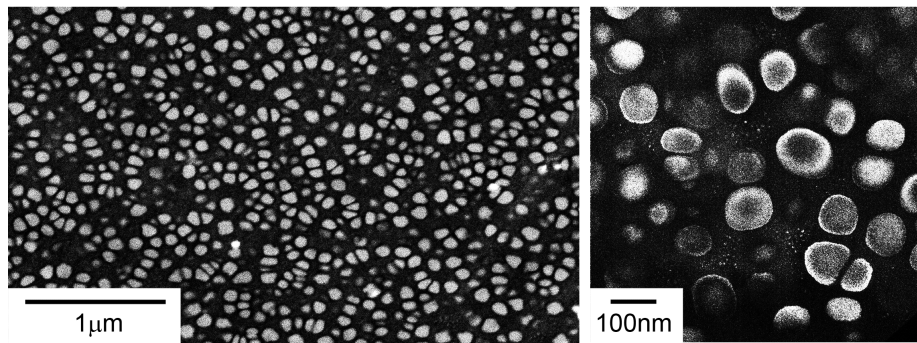


Figure 7: Micrographs of the  $\gamma'$  particles in the (a) forged condition, (b) sub-solvus SST and air cooled condition, and (c) the sub-solvus SST and furnace cooled condition. The left images are SEM backscatter micrographs and the right images are conventional TEM micrographs. The SEM micrographs show the primary precipitates, whilst the TEM micrographs show both the secondary and tertiary precipitates.

(a) Super-Solvus SST and air cool



(b) Super-Solvus SST and furnace cool

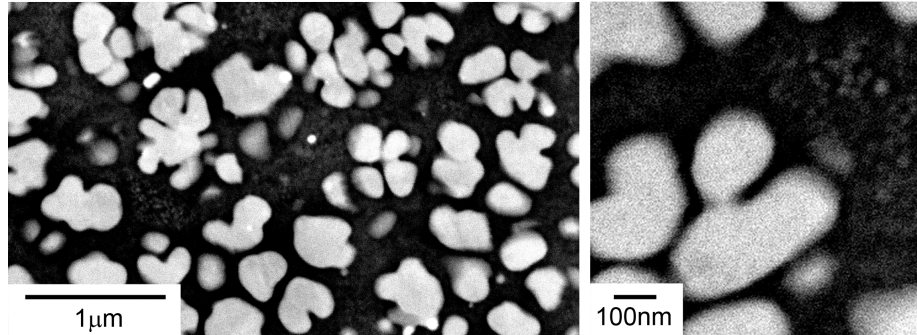


Figure 8: Micrographs of the  $\gamma'$  particles in the (a) super-solvus SST and air cooled condition, and (b) the super-solvus SST and furnace cooled condition. The top right image is taken from a conventional TEM sample, whilst the others are backscatter SEM micrographs.

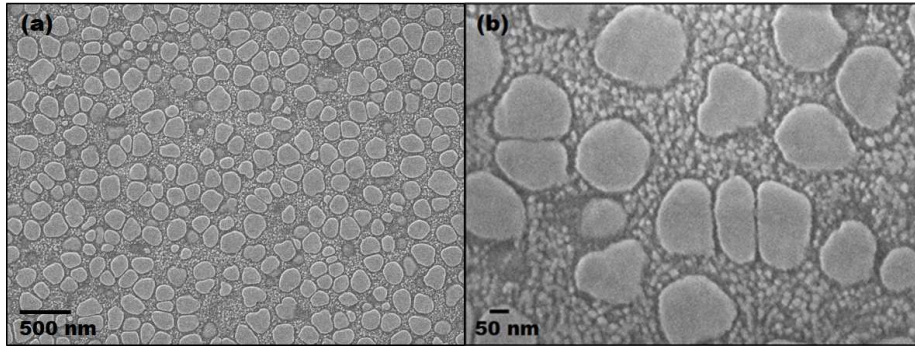


Figure 9: SEM secondary electron images of the as-received coarse grain RR1000 specimens showing (a) the secondary particles, and (b) the tertiary particles.

are summarised in Table 3. The secondary precipitates show small changes in size after 500h of aging at 700°C. Noticeable coarsening of the secondary precipitates is observed during isothermal aging at 800°C. At 700°C and 750 °C the tertiary particles increase in size during isothermal aging within an exposure time of 500h. At 800°C the tertiary precipitates have increased in mean size after 100h, however have dissolved after 500h. At 700°C a small increase in tertiary volume fraction is observed, however after an exposure of 500h at this temperature, there is no significant change. At 750°C, the tertiary dissolves significantly, reducing from 9% to 2.7% after 500h. The tertiary precipitates have fully dissolved after 500h at 800°C.

Figure 12a) presents the predicted equilibrium property diagram for RR1000, using the thermodynamic database TTNi8. The equilibrium volume fractions at 700 °C, 750°C and 800°C shown in Figure 12 are 46.2%, 45.3%, and 44.1%, respectively. The dissolution observed in the tertiary  $\gamma'$  can be partially attributed to the reduction in equilibrium  $\gamma'$  phase fraction with an increase in temperature, with the thermodynamic database suggesting a 2.1% drop in equilibrium phase fraction considering the temperature range of interest. The remaining reduction in volume fraction of tertiary  $\gamma'$  volume fraction is likely a result of competitive growth between secondary and tertiary precipitates.

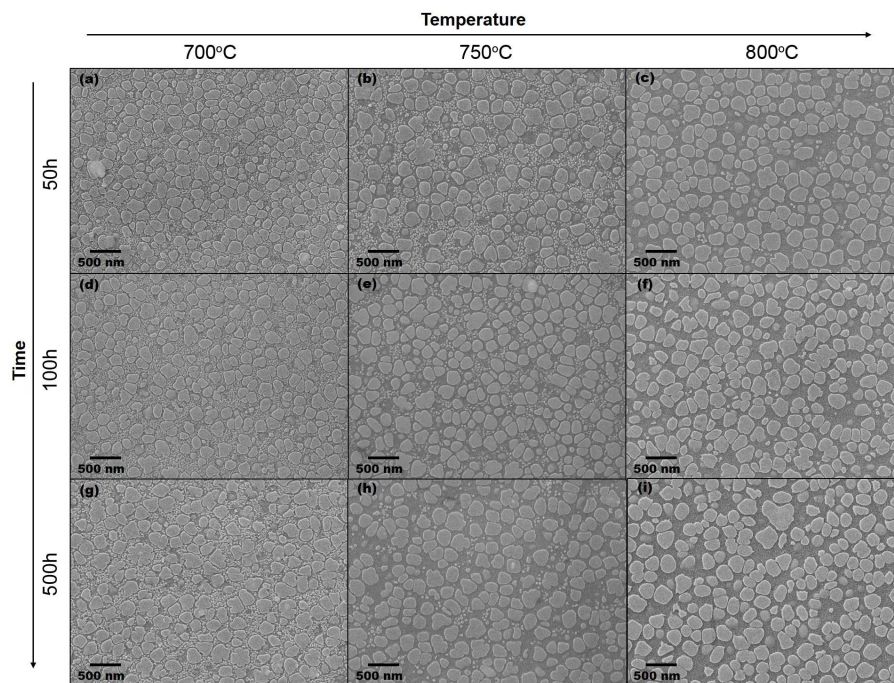


Figure 10: SEM secondary electron images of the secondary  $\gamma'$  after isothermal aging coarse-grain RR1000 for different times and temperatures.

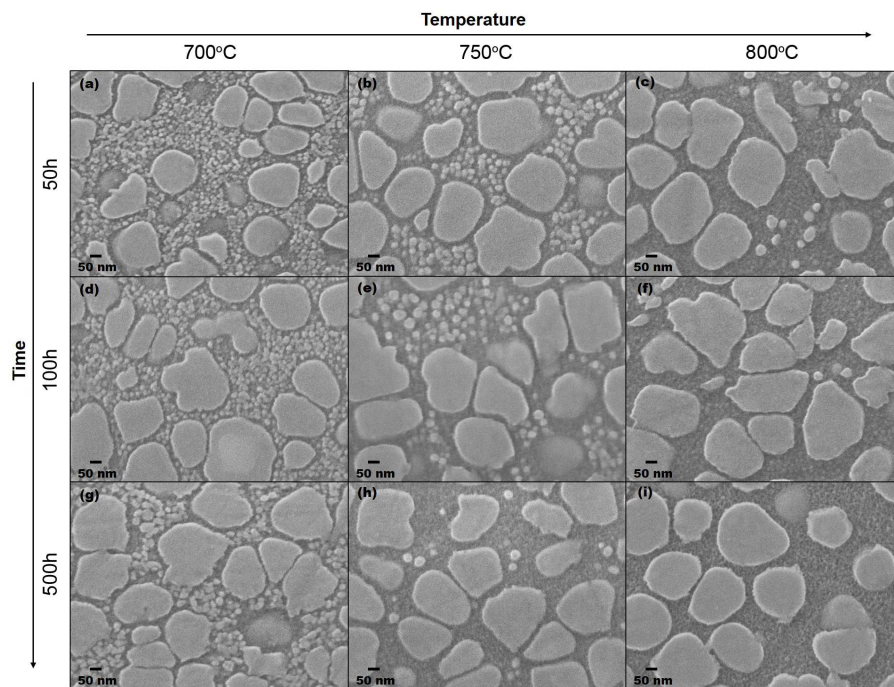


Figure 11: SEM secondary electron images of the tertiary  $\gamma'$  after isothermal aging coarse-grain RR1000 for different times and temperatures.

Table 3: Summary of the  $\gamma'$  measurements taken from isothermally aged coarse grain RR1000. Some of the measurements have been obtained by quantitative analysis of TEM micrographs, whilst others from SEM micrographs.

Condition	Measurement technique	Secondary		Tertiary	
		$\phi$ (%)	$\langle R \rangle$ (nm)	$\phi$ (%)	$\langle R \rangle$ (nm)
As-received	TEM	37.8	87.0	8.3	10.5
700°C for 50h	TEM	36.6	88.5	9.4	11.5
700°C for 100h	TEM	36.2	91.0	9.9	13.5
700°C for 500h	TEM	37.3	99.5	8.8	16.5
750°C for 50h	SEM	36.0	103.0	9.0	17.0
750°C for 100h	TEM	39.8	94.5	5.2	20.5
750°C for 500h	SEM	42.3	101.5	2.7	23.5
800°C for 50h	SEM	42.0	97.5	1.5	25.0
800°C for 100h	TEM	42.7	101.0	0.8	30.0
800°C for 500h	SEM	43.5	112.0	0.0	0.0

### 3. Numerical modelling

#### 3.1. Mean-field modelling

In this modelling approach, the particles are treated as spherical with their growth rate a function of the particle size and the composition of the matrix and particle phases. Let the distribution function  $\mathcal{F}(R, t)dR$  describe the three dimensional radius of the particle distribution at a given time,  $t$ . Statistical information of interest regarding the particle dispersion is calculated from moments of  $\mathcal{F}(R, t)$  with respect to  $R$

$$\begin{aligned}
 N_v(t) &= \int_0^\infty \mathcal{F}(R, t) dR \\
 \langle R(t) \rangle &= \int_0^\infty R \mathcal{F} dR \left[ \int_0^\infty \mathcal{F}(R, t) dR \right]^{-1} \\
 \phi(t) &= \frac{4\pi}{3} \int_0^\infty R^3 \mathcal{F}(R, t) dR
 \end{aligned} \tag{9}$$

The evolution of the particle distribution is determined by solving the continuity equation

$$\frac{\partial \mathcal{F}(R, t)}{\partial t} + \frac{\partial \mathcal{F}(R, t)V(R, t)}{\partial R} = \dot{\mathcal{J}}^+(R, t) - \dot{\mathcal{J}}^-(R, t) \quad (10)$$

where  $\dot{\mathcal{J}}^+(R, t)$  and  $\dot{\mathcal{J}}^-(R, t)$  refer to source and sink terms respectively. The generalised particle growth rate descriptive of Ostwald ripening kinetics is

$$V(R, t) = \frac{A(t)}{R} \left( \frac{1}{R_c(t)} - \frac{1}{R} \right) z(R, t) \quad (11)$$

where the term  $A(t)$  includes the rate of diffusion of alloying elements at the particle-matrix interface. The term  $R_c$  is the critical particle radius, with particles smaller than this value dissolving and those larger growing. The term  $z(R, t)$  accounts for the impact of the overlap of diffusion fields between neighbouring particles, accelerating particle growth kinetics. Marqusee and Ross [29] derived the following correction factor

$$z(R, t) = 1 + R\sqrt{4\pi N_v \langle R \rangle} \quad (12)$$

A description of the nucleation rate may be obtained from classical nucleation theory, considering homogenous nucleation of spherical particles [30]. The transient nucleation rate is given by Anderson *et al.* [14],

$$\dot{\mathcal{J}}^+(R, t) = Z\beta^* N_c(R) \exp\left(\frac{-\Delta G^*}{k_b T}\right) P_{inc} \quad (13)$$

where the  $Z$  term refers to the Zeldovitch factor,  $\beta^*$  is the atomic attachment rate,  $N_c(R)$  is the number density concentration of nuclei, and  $\Delta G^*$  is the nucleation barrier. The terms  $k_b$  and  $T$  refer to the Boltzmann constant and the absolute temperature respectively.  $P_{inc}$  is the nuclei incubation probability and is given by

$$P_{inc} = \exp\left(\frac{-\tau}{t}\right) \quad (14)$$

where  $\tau$  is the incubation time.

### 3.2. Particle nucleation

To implement a classical description of nucleation, expressions for the nucleation barrier,  $\Delta G^*$ , the atomic attachment rate,  $\beta^*$  and the number density of

nuclei,  $N_c$  are needed. This model makes use of Svoboda *et al.*'s [10] description of the atomic attachment rate and uses the Gaussian waveform adopted by Jou *et al.* [12] to describe the distribution of nuclei.

The nucleation barrier for spherical particles is

$$\Delta G^{*} = \frac{16\pi}{3} \frac{\sigma^3}{(\Delta G_c - U)^2} \quad (15)$$

where  $U$  is the misfit strain energy and  $\Delta G_c$  is the chemical driving force

$$\Delta G_c = - \sum_{i=1}^n c_{ki} (\mu_{ki} - \mu_{0i}) \quad (16)$$

$\mu_{ki}$  and  $\mu_{0i}$  are the chemical potentials of the particle and matrix phases, respectively, for an alloy containing  $n$  many alloying elements. The chemical composition of the  $i$ th alloying element within the matrix and particle is given by  $c_{0i}$  and  $c_{ki}$ , respectively.

The misfit strain energy is approximated by

$$U = \frac{\varepsilon_0^2 E}{(1 - \nu)} \quad (17)$$

where  $E$  is the Young's modulus,  $\nu$  is Poisson's ratio, and  $\varepsilon_0$  is the misfit volume strain. Svoboda *et al.*'s [10] approximation of a multicomponent atomic attachment rate is given by

$$\beta^* = \frac{4\pi R_c^2}{a^4 V_m} \theta \quad (18)$$

where  $R_c$  is the critical particle radius,  $a$  is the lattice parameter and  $V_m$  is the molar volume. The term  $\theta$  is given by

$$\theta = \left[ \sum_{i=1}^n \frac{(c_{ki} - c_{0i})^2}{c_{0i} D_{0i}} \right]^{-1} \quad (19)$$

where  $D_{0i}$  is the diffusivity of the  $i$ th element in the matrix. Jou *et al.* [12] used the Gaussian waveform shown in equation 20 to describe the distribution of nuclei, where  $N_0$  is the concentration of nuclei sites and  $\delta$  is the variance of the nuclei size distribution.

$$N_c(R) = \frac{N_0}{\delta\sqrt{2\pi}} \exp\left(-\frac{(R - R_c)^2}{2\delta^2}\right) \quad (20)$$

An expression for  $\delta$  may be obtained from the Zeldovitch parameter. The Zeldovitch parameter is descriptive of the flatness of  $\partial G/\partial R$  at  $R_c$  and is given by

$$Z = \sqrt{\frac{\Omega^2 \sigma}{4\pi^2 k_B T R_c^4}} \quad (21)$$

where  $k_B$  is Boltzmann's constant and  $\Omega$  is the atomic volume. It is calculated by considering the width,  $\Delta R$ , of a thermal fluctuation  $k_b T$  from  $R_c$ . The variance may be related to  $\Delta R$ , as shown in equation 22.

$$\delta = \left( \frac{3\Omega}{2(\pi)^{3/2} Z} \right)^{\frac{1}{3}} \quad (22)$$

The temporal evolution of the incubation probability is determined from Anderson *et al.* [14]

$$\frac{dP_{\text{inc}}}{dt} = \frac{\tau}{t_{\text{eq}}} P_{\text{inc}} \left[ \frac{1}{t_{\text{eq}}} + \left( \frac{1}{\theta} \frac{d\theta}{dT} - \frac{2}{R_c} \frac{dR_c}{dT} + \frac{1}{\sigma} \frac{d\sigma}{dT} - 1 \right) \frac{dT}{dt} \right] \quad (23)$$

where  $P_{\text{inc}}(t) > 0$  and  $P_{\text{inc}}(t) < 1$ . The term  $t_{\text{eq}}$  is the equivalent incubation time for the conditions of interest

$$t_{\text{eq}} = -\frac{\tau}{\ln(P_{\text{inc}})} \quad (24)$$

### 3.3. The particle growth rate

Svoboda *et al.*'s [10] derived a multi-component description of precipitation kinetics by considering  $N$  moles with  $n$  many alloying elements and a dispersion containing  $m$  many particles. This approach has been extended to include more detail regarding the concentration gradients within the matrix during regimes of nucleation and growth. Svoboda *et al.*'s [10] particle growth rate is obtained from the application of the thermodynamic extremum principle [10], which states that

$$\frac{\partial G}{\partial R_k} = -\frac{1}{2} \frac{\partial Q}{\partial \dot{R}_k} \quad (25)$$

where  $G$  is the Gibbs energy and  $R_k$  is the radius of the  $k$ th particle.  $\dot{R}_k$  is the growth rate of the  $k$ th particle and  $Q$  is the total rate of Gibbs energy dissipation given by  $Q = Q_1 + Q_2 + Q_3$ . The three contributions to the rate of dissipation of the Gibbs free energy considered by Svoboda *et al.*'s [10] are

1. The migration of interfaces driven by the mobility of the interfaces.
2. The diffusion of chemical species within the precipitate.
3. The diffusion of chemical species within the matrix.

The dissipation rates are given by

$$\begin{aligned}
Q_1 &= \sum_{k=1}^m \frac{4\pi R_k^2 \dot{R}_k^2}{M_k} \\
Q_2 &= \sum_{k=1}^m \sum_{i=1}^n \frac{4\pi R_g T R_k^5 \dot{c}_{ki}^2}{45 c_{ki} D_{ki}} \\
Q_3 &= \sum_{k=1}^m \sum_{i=1}^n \int_{R_k}^Z \frac{R_g T}{c_{0i} D_{0i}} 4\pi r^2 J_{ki}^2 dr
\end{aligned} \tag{26}$$

where  $M_k$  is the mobility of the interface,  $R_g$  is the gas constant, and  $T$  is the absolute temperature. Similarly, the diffusivity of the  $i$ th alloying element is given by  $D_{0i}$  and  $D_{ki}$  for the matrix and particle phases. The third rate of dissipation,  $Q_3$ , describes the dissipation of the Gibbs free energy through diffusion of species within the matrix. Let  $x$  describe the distance from the particle centre of particle  $R_k$ . The diffusive flux entering the particle is assumed to be radial and approximated by

$$J_{ki} = J_{ki}^* \frac{R_k^2}{x^2} \frac{Z^3 - x^3}{Z^3 - R_k^3} \tag{27}$$

where  $x$  varies between  $R_k$  and  $Z$ . The distance  $Z$  defines the concentration gradient created by solutes absorbed or emitted by the particle within the matrix. Substituting Equation 27 into  $Q_3$  in Equation set 26 gives,

$$Q_3 = \sum_{k=1}^m \sum_{i=1}^n \frac{R_g T}{c_{0i} D_{0i}} 4\pi (J_{ki}^*)^2 R_k^4 \int_{R_k}^Z \frac{1}{x^2} \left( \frac{Z^3 - x^3}{Z^3 - R_k^3} \right)^2 dx \tag{28}$$

The distance  $Z$  can be calculated as a function of the super-saturation of particle forming species [31]. Let  $Z = R(1 + \xi_i)$ , where  $\xi_i$  is given by  $\xi_i = \omega_i/(2\lambda_i)$  and accounts for the diffusion distance as described by Chen *et al.* [8]. The term is modified to describe the distance from the particle centre.  $\omega_i$  is the dimensionless super-saturation and is given by,

$$\omega_i = \frac{c_{0i} - \bar{c}_{0i}}{\bar{c}_{ki} - \bar{c}_{0i}} \tag{29}$$

where  $\bar{c}_{0i}$  and  $\bar{c}_{ki}$  are compositions at the particle-matrix interface within the matrix and particle, respectively. The term  $\lambda_i$  is calculated to satisfy

$$2\lambda_i - 2\lambda_i^3 \sqrt{\pi} \exp(\lambda_i^2) \operatorname{erfc}(\lambda_i) = \omega_i \quad (30)$$

Svoboda *et al.*'s [10] provide the following approximation of the flux at the particle-matrix interface

$$J_{ki}^* = \dot{R}_k (c_{ki} - c_{0i}) + \frac{R_k \dot{c}_{ki}}{3} \quad (31)$$

Equation 31 can then be substituted into Equation 28. The diffusion distance is defined by  $Z = R(1 + \xi_i) = R\Lambda_i$ , resulting in the following solution for the integral

$$Q_3 = \sum_{k=1}^m \sum_{i=1}^n \frac{R_g T}{c_{0i} D_{0i}} 4\pi R_k^3 \chi_i \left( \dot{R}_k (c_{ki} - c_{0i}) + \frac{R_k \dot{c}_{ki}}{3} \right)^2 \quad (32)$$

$$\chi_i = \frac{\Lambda_i^6 - 9/5 \Lambda_i^5 + \Lambda_i^3 - 1/5}{(\Lambda_i^3 - 1)^2}$$

The total rate of dissipation of the Gibbs energy is now given by

$$Q = \sum_{k=1}^m \frac{4\pi R_k^2 \dot{R}_k^2}{M_k} + \sum_{k=1}^m \sum_{i=1}^n \frac{4\pi R_g T R_k^5 \dot{c}_{ki}^2}{45 c_{ki} D_{ki}} \quad (33)$$

$$+ \sum_{k=1}^m \sum_{i=1}^n \frac{R_g T}{c_{0i} D_{0i}} 4\pi R_k^3 \chi_i \left( \dot{R}_k (c_{ki} - c_{0i}) + \frac{R_k \dot{c}_{ki}}{3} \right)^2$$

The partial derivative of Equation 33 with respect to  $\dot{R}_k$  is

$$\frac{\partial Q}{\partial \dot{R}_k} = \sum_{k=1}^m \frac{8\pi R_k^2 \dot{R}_k}{M_k} + \sum_{i=1}^n \frac{R_g T}{c_{0i} D_{0i}} 4\pi R_k^3 \dot{R}_k \chi_i (c_{ki} - c_{0i})^2 \quad (34)$$

$$+ \frac{8\pi R_g T R_k^4}{3} \sum_{i=1}^n \frac{\chi_i (c_{ki} - c_{0i}) \dot{c}_{ki}}{c_{0i} D_{0i}}$$

The partial derivative of the Gibbs free energy with respect to  $R_k$  is

$$\frac{\partial G}{\partial R_k} = 8\pi R_k \sigma + 4\pi R_k^2 (\Delta G_c - U) \quad (35)$$

The particle growth rate is obtained by substituting Equations 35 and 34 into Equation 25, and then rearranging for  $\dot{R}_k$ .

Assuming that  $\dot{c}_{ki}$  has a negligible impact upon the particle growth rate [10], the following parameters for the generic particle growth rate described in Equation 11 are obtained

$$\begin{aligned} R_c &= \frac{2\sigma}{\Delta G_c - U} \\ A &= \frac{2\sigma}{R_g T} \theta \end{aligned} \quad (36)$$

The term  $\theta$  is now updated to include  $\chi_i$

$$\begin{aligned} \theta &= \left[ \sum_{i=1}^n \frac{\chi_i (c_{ki} - c_{0i})^2}{c_{0i} D_{0i}} \right]^{-1} \\ \chi_i &= \frac{\Lambda_i^6 - 9/5 \Lambda_i^5 + \Lambda_i^3 - 1/5}{(\Lambda_i^3 - 1)^2} \end{aligned} \quad (37)$$

The modified term can be used within the atomic attachment rate, shown in Equation 18. Setting  $\chi_i = 1$  recovers Svoboda *et al.*'s [10] original particle growth rate.

#### 3.4. Isolated tertiary particles

The measured coarsening kinetics during isothermal aging presented in Figures 11 show that during aging at 700°C the tertiary particles are relatively stable under conditions where Ostwald ripening would suggest they should dissolve.

Mean-field models assume that the diffusion within the matrix has reached a quasi-static state, however Singh *et al.* [32] and Li *et al.* [17] have observed differences in chemical composition in the matrix comparing different particle populations when examining quenched specimens of the nickel based superalloy Rene88DT and FGH96, respectively. Li *et al.* [17] and Radis *et al.* [18] observed depletion zones surrounding the secondary particles with the tertiary particles nucleating the super-saturated regions between secondary precipitates. The different matrix and particle chemistries considering the secondary and tertiary environments would alter the chemical driving force for the particle populations, impacting the stability of the tertiary precipitates. Until the depletion zones within the matrix homogenise, the secondary and tertiary precipitates would not

be in direct competition. Tertiary free zones surrounding the secondary particles can be observed in Figure 11. Chen *et al.* [4] measured significant differences in composition between the secondary and tertiary particles in quenched RR1000, suggesting that similar behaviour occurs in RR1000.

A phenomenological model has been developed to capture the formation of isolated pockets of tertiary which do not directly compete with secondary particles for solute. Let  $\eta$  describe the fraction of isolated tertiary. It is assumed that  $\eta$  evolves through diffusion using an Avrami expression as shown below

$$\begin{aligned}\eta(t) &= \exp(-\mathcal{K}t^n) \\ \mathcal{K} &= D_0 \exp\left(\frac{-Q_v}{R_g T}\right)\end{aligned}\quad (38)$$

where  $D_0$ ,  $Q_v$ , and  $n$  are the diffusivity constant, activation energy and the exponent term which define how the fraction of isolated tertiary evolve with time. The temporal evolution is given by

$$\begin{aligned}\dot{\eta}(t) &= -\mathcal{K} n t_{eq}^{n-1} \eta(t) \\ t_{eq} &= \left(\frac{-\log(\eta)}{\mathcal{K}}\right)^{\frac{1}{n}}\end{aligned}\quad (39)$$

where  $\eta(t) > 0$  and  $\eta(t) < 1$ .

Let the  $\gamma'$  precipitates be split into separate distribution functions to distinguish the primary, secondary, tertiary, and isolated tertiary precipitate, given by  $\mathcal{F}_p$ ,  $\mathcal{F}_s$ ,  $\mathcal{F}_t$ , and  $\mathcal{F}_t^*$  respectively. It is assumed that during nucleation,  $\eta = 1$ , and  $\eta$  only evolves when  $R_c > \langle R_t^* \rangle$ , where  $\langle R_t^* \rangle$  is the mean size of the isolated tertiary precipitates. All nucleated tertiary precipitates are assumed to be isolated. When  $\eta$  is evolving, the kinetics of the isolated tertiary particles are given by

$$\frac{\partial \mathcal{F}_t^*(R, t)}{\partial t} + \frac{\partial \mathcal{F}_t^*(R, t) V^*(R, t)}{\partial R} = \dot{\mathcal{F}}_t^{*+}(R, t) - \dot{\mathcal{F}}_t^{*-}(R, t) - \dot{\mathcal{Q}}^-(R, t) \quad (40)$$

where  $\dot{\mathcal{F}}_t^{*+}(R, t)$  and  $\dot{\mathcal{F}}_t^{*-}(R, t)$  are source and sink terms describing the nucleation and the dissolution of tertiary particles, respectively. The term  $\dot{\mathcal{Q}}^-(R, t)$

is a sink term and describes the rate at which isolated tertiaries start to interact directly with the rest of the precipitate dispersion, and is approximated by

$$\dot{Q}^-(R, t) = -\dot{\eta} \mathcal{F}_t^*(R, t) \quad (41)$$

A complementary source term is added to the advection equation for tertiary particles,  $\mathcal{F}_t(R, t)$

$$\frac{\partial \mathcal{F}_t(R, t)}{\partial t} + \frac{\partial \mathcal{F}_t(R, t)V(R, t)}{\partial R} = -\dot{\mathcal{F}}_t^-(R, t) + \dot{Q}^+(R, t) \quad (42)$$

where  $\dot{Q}^+(R, t) = -\dot{Q}^-(R, t)$ . The isolated tertiary precipitates are assumed to evolve following their own particle growth rate

$$V^*(R, t) = \frac{A^*(t)}{R} \left( \frac{1}{R_c^*(t)} - \frac{1}{R} \right) z(R, t) \quad (43)$$

where  $A^*(t) = \mathcal{C}A(t)$ . The constant  $\mathcal{C}$  was introduced to reflect the impact of different local chemistries and thus thermodynamic states considering the regions of isolated tertiary precipitates compared to the rest of the dispersion.

The critical particle radius of the isolated tertiary precipitates is calculated assuming conservation of solute within the isolated tertiary particles and thus a constant isolated tertiary volume fraction. For a particle growth rate that can be expressed in the generic form shown in Equation 43, the critical particle radius assuming a constant volume fraction is

$$R_c^*(t) = \frac{\int_0^\infty \mathcal{F}_t^*(R, t) R z(R, t) dR}{\int_0^\infty \mathcal{F}_t^*(R, t) z(R, t) dR} \quad (44)$$

For a dilute volume fraction of precipitates,  $z(R, t)$  approaches unity, and the critical particle radius of a coarsening dispersion is given by the mean particle radius. The derivation of Equation 44 is presented in the appendix.

#### 4. Implementation

The chemical potentials and diffusivities needed for the precipitation calculations have been obtained from the TTNi8 thermodynamic database combined

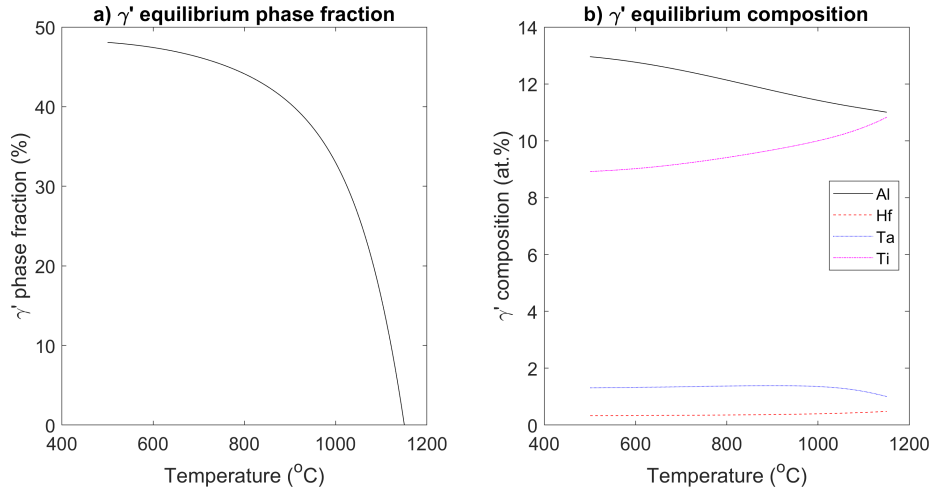


Figure 12: a) The predicted equilibrium property diagram for the  $\gamma'$  and  $\gamma$  phases using the composition in Table 4 and the thermodynamic database TTNi8. b) The predicted  $\gamma'$  equilibrium composition for  $\gamma'$  forming elements using the TTNi8 database.

Table 4: Simplified chemical composition of RR1000 (at%)

Al	Co	Cr	Hf	Mo	Ni	Ta	Ti	Zr
6.35	17.94	16.49	0.16	2.98	bal	0.63	4.29	0.04

with the MOBNI1 mobility database. The calculations have been performed using the TQ FORTRAN interface in the commercial software ThermoCalc [33]. A simplified chemical composition descriptive of RR1000 has been used, and is presented in Table 4.

The  $\gamma'$  property diagram and predicted equilibrium composition of  $\gamma'$  formers are shown in Figure 12 a) and b), respectively. The predicted precipitate compositions are in reasonable agreement with the experimental measurements of Kitaguchi *et al.* [34]. The calculations apply an energy contributions of -71.38J/mol to the  $\gamma'$  phase to obtain a solvus temperature of  $\sim 1150^\circ\text{C}$ .

The model parameters are given in Table 5, where the variable  $\mathcal{C}$  is used in Equation set 43. The interfacial energy, Young modulus, and Poisson's ratio have been implemented using polynomials as a function of absolute temperature. The polynomial coefficients are given in Table 6, and use the polynomial

expression in in Equation 45.

$$x = \sum_{i=0}^n a_i T^i \quad (45)$$

The mean-field model is implemented by solving the following continuity equations for primary, secondary, isolated tertiary, and tertiary particles, respectively

$$\begin{aligned} \frac{\partial \mathcal{F}_p(R, t)}{\partial t} + \frac{\partial \mathcal{F}_p(R, t)V(R, t)}{\partial R} &= -\dot{\mathcal{F}}_p(R, t)^+ \\ \frac{\partial \mathcal{F}_s(R, t)}{\partial t} + \frac{\partial \mathcal{F}_s(R, t)V(R, t)}{\partial R} &= \mathcal{H} \dot{\mathcal{F}}_s^+(R, t) - \dot{\mathcal{F}}_s^-(R, t) \\ \frac{\partial \mathcal{F}_t^*(R, t)}{\partial t} + \frac{\partial \mathcal{F}_t^*(R, t)V^*(R, t)}{\partial R} &= (1 - \mathcal{H}) \dot{\mathcal{F}}_t^{*+}(R, t) - \dot{\mathcal{F}}_t^{*-}(R, t) - \dot{\mathcal{Q}}^-(R, t) \\ \frac{\partial \mathcal{F}_t(R, t)}{\partial t} + \frac{\partial \mathcal{F}_t(R, t)V(R, t)}{\partial R} &= -\dot{\mathcal{F}}_t^-(R, t) + \dot{\mathcal{Q}}^+(R, t) \end{aligned} \quad (46)$$

The model requires the initial PRD functions for each type of precipitate and simulates the nucleation of secondary and tertiary particles during a solid-solution treatment. The term  $\mathcal{H}$  is a Heaviside step function used to determine the transition from nucleating isolated tertiary particles instead of secondary particles. The default value for  $\mathcal{H}$  is unity, and has a value of zero depending upon two criteria; The first criteria used to determine whether to make the transition from secondary to tertiary particle nucleation is to check whether the mean size of the secondary particles has exceeded 25nm. Another criteria uses the combination of the secondary volume fraction exceeding 1% and the mean secondary particle radius exceeding 5nm. If any of the criteria are met, isolated tertiary particles are nucleated rather than secondary particles with  $\mathcal{H} = 0$ .

It is assumed that the diffusion fields within the locations of isolated tertiary precipitates are relatively flat so that the  $z(R, t)$  factor for isolated tertiary precipitates is approximated by unity, and in addition  $\chi_i$  for the isolated tertiary precipitates is also approximated by unity. The mean particle radius and particle concentration that enters the  $z(r, t)$  factor shown in Equation 12 uses moments taken of the combined primary, secondary, and tertiary particle distribution

Table 5: Model parameters: The temperature dependence of the interfacial energy,  $\sigma$ , is given in Kelvin.

Variable	Value	Units
$M_v$	7.44E-06	m <sup>3</sup> /mol
$\mathcal{C}$	0.5	dimensionless
$D_v$	2.0e24	1/s
$Q_v$	650	kJ/mol
$n$	1.5	dimensionless

Table 6: Polynomial coefficients for the interfacial energy  $\sigma$ , the Young modulus  $E$ , the Poisson's ratio  $\nu$ , and the lattice misfit  $\varepsilon_0$ . The interfacial energy is given in  $Jm^{-2}$ , and the Young modulus in  $GPa$ . The temperature dependencies are given in Kelvin.

	$a_0$	$a_1$	$a_2$	$a_3$	$a_4$
$\sigma$	4.78103908E-02	-2.66430E-05	0	0	0
$E$	1.9829E+02	2.1467E-01	-5.8385E-04	5.1745E-07	-1.6877E-10
$\nu$	2.4545E-01	4.0896E-04	-5.2834E-07	2.4370E-10	-1.7328E-15
$\varepsilon_0$	9.95844E-04	- 6.90512E-07	- 1.38068E-09	1.55934E-12	-3.31439E-16

functions, omitting the isolated tertiary particles.

The continuity equations, particle growth rates, and the nucleation rate are normalised and reformulated following the method outlined by Anderson *et al.* [14]. The advection equations are solved using finite difference, using the scheme described by Anderson *et al.* [13]. The method used to describe nucleation follows that of Jou *et al.* [12], using a distribution functions to describe the variation in size of stable nuclei. This requires a sufficiently fine discretization of the particle radius distribution function to capture the nuclei distribution accurately.

## 5. Results

### 5.1. Solid solution treatment

The model described in section 3 has been applied using the parameters outlined in section 4 to the heat treatments shown in Figure 6. A comparison of the model predictions and measurements is shown in Figures 14 and 15, considering a sub-solvus SST and super-solvus SST respectively. The initial microstructure is in the as-forged condition, shown in Figure 7 a).

The Figures display the PRDs using both  $G_{2D}$  and  $G_{3D}$  formulations using Equations 7 and 8, respectively. Figure 13 presents the approximated 3D PRD of the as-forged condition for use in simulation. Figures 14 a) and b) compare the model predictions with experimental data for the air-cooled specimen, whilst figures c) and d) is a comparison of the furnace cooled condition. Figures b) and d) compare predictions with SEM measurements, calculating the 2D PRD from the predicted primary dispersion. Figure 15 a) compares the predicted and measured distribution for the air-cool after a super-solvus SST, whilst Figure b) presents the comparison for the furnace cool.

The model captures the primary particle PRDs with good agreement, however under predicts the size of the secondary particle population in the sub-solvus conditions. The model is more accurate in capturing the mean sizes of the secondary and tertiary particles in the super-solvus conditions. In all predictions, the shape of the predicted dispersions are narrower compared to measurements.

The model helps rationalise the kinetics of the secondary and tertiary precipitates detailed in section 2.3. The predicted evolution of the  $\gamma'$  forming alloy elements in the matrix during quenching is presented in Figure 16, where Figure 16 a) and b) present the predictions for super-solvus SSTs, and Figures c) and d) describe the sub-solvus SSTs. The initial matrix super-saturation is higher in the super-solvus heat treatments compared to the sub-solvus conditions, due to the presence of primary particles that reduce the solute available to form secondary and tertiary precipitates. For Figure 16 a) and b), the reduction in matrix

super-saturation corresponds with the nucleation of precipitates. For Figure 16 c) and d), the growth of primary particles absorbs matrix super-saturation, reducing the amount of solute and chemical driving force for nucleation.

The impact of the primary precipitates is reflected in the temperature at which the secondary and tertiary precipitates are predicted to nucleate, which is presented in Table 7. For the super-solvus conditions, the secondary precipitates nucleate at a temperature of  $\sim 1142^{\circ}\text{C}$ , and in the sub-solvus conditions the secondary precipitates nucleate at  $\sim 1110^{\circ}\text{C}$ . The secondary precipitates in the air cooled conditions are predicted to nucleate at temperatures  $\sim 2^{\circ}\text{C}$  lower than the furnace cooled conditions. The small delay is a result of the incubation time which has a greater impact upon quenches that have a faster cooling rate.

The secondary precipitates during the furnace cooled conditions are predicted to nucleate and grow quickly to reach the equilibrium volume fraction. As the temperature drops, the particles reach a state where their continued growth cannot keep up with the increase in matrix super-saturation of precipitate forming solute. When the matrix solute super-saturation reaches a sufficient amount and the chemical driving force is large enough, the tertiary precipitates begin to nucleate and grow.

The tertiary precipitates are predicted to nucleate at higher temperatures in the air quenched condition ( $815\text{-}830^{\circ}\text{C}$ ) compared to the furnace cooled conditions ( $650\text{ - }690^{\circ}\text{C}$ ). Despite the tertiary nucleating at a higher temperature in the air cooled conditions, the tertiary in the furnace cooled conditions are predicted to grow to larger mean sizes in comparison to the air cooled condition. This is because the tertiary in the furnace cooled conditions are exposed to temperatures where they can grow and coarsen for a greater duration of time.

The measurements indicate a larger volume fraction of tertiary particles in the furnace cooled super-solvus condition compared to the furnace cooled sub-solvus furnace cooled condition. The model suggests that this may be due to the significantly larger secondary particles in the super-solvus furnace cooled condition whose growth kinetics would be sluggish, allowing for a greater build up of super-saturation of precipitate forming solutes, and thus more tertiary

Table 7: The predicted temperature at which the secondary and tertiary precipitate populations nucleate.

Heat treatment	Nucleation temperature ( $\backslash$ degree C)	
	Secondary particles	Tertiary particles
Super-solvus SST + Air quench	1142.4	827.8
Super-solvus SST + Furnace quench	1143.7	689.9
Sub-solvus SST + Air quench	1108.6	816.7
Sub-solvus SST + Furnace quench	1111.1	648.4

precipitates. The smaller secondary particles in the sub-solvus condition would be able to grow and absorb more solute during the quench in comparison to the super-solvus furnace cooled condition.

### 5.2. Aging

The initial coarse-grain RR1000 microstructure is shown in Figure 9. The approximated 3D PRD of the secondary and tertiary particle populations is shown in Figure 17. The predicted aging behaviour of this dispersion is presented in Figure 18, comparing measured and predicted PRDs. The model predictions and tertiary data obtained from TEM has been converted into  $F_{2D}$  using Equation 6. The results shown in Figure 9 are shown in the area fraction reformulation given in Equation 7. The model captures the coarsening of both the secondary and tertiary particle populations with reasonable accuracy. The shape of the tertiary particle radius distribution shown in Figure 18 c) is not captured. The wider bimodal distribution of tertiary may be a result of coalescence.

## 6. Discussion

### 6.1. Tertiary precipitate kinetics

Figure 19 compares the predicted and measured volume fraction of tertiaries during isothermal aging of as-heat treated coarse grain RR1000. Two variants of the model are presented; one with the phenomenological treatment of

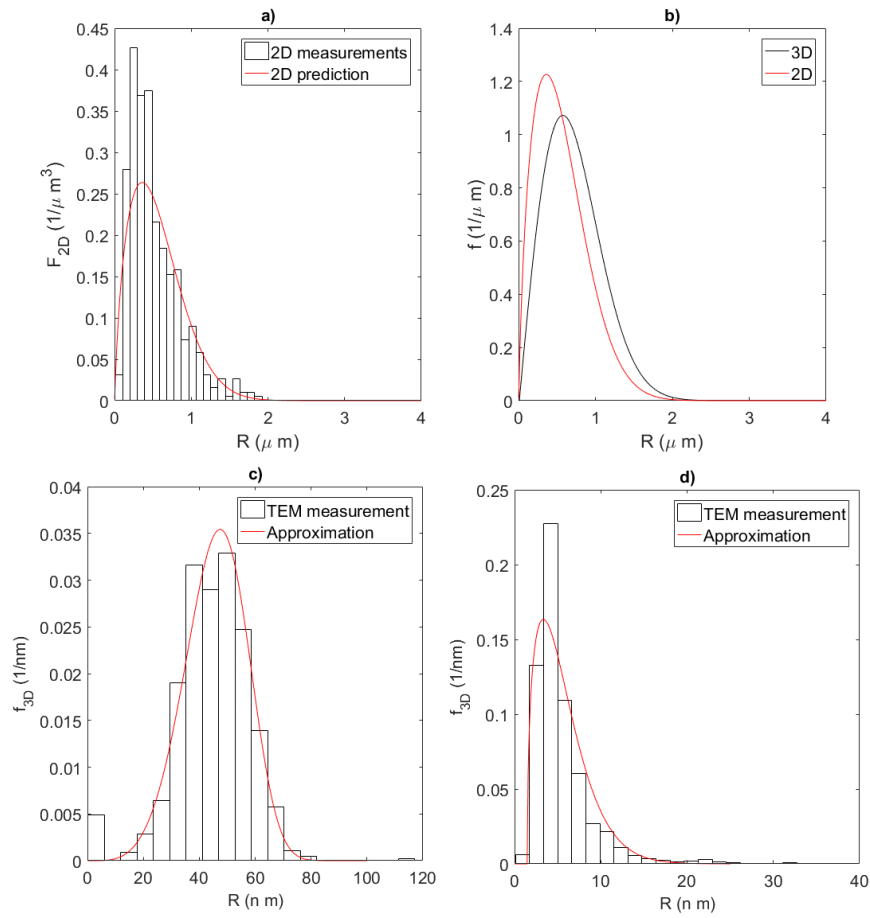


Figure 13: The approximated 3D PRD in the as-forged condition. Figure a) compares the measured primary PRD from SEM micrographs with the approximated PRD of particle cross sections. Figure b) presents the approximated 3D PRD for primary particles, showing the associated PRD of cross sections. Figures c) and d) presents the approximated 3D PRDs for secondary and tertiary particle populations, respectively, using TEM micrographs.

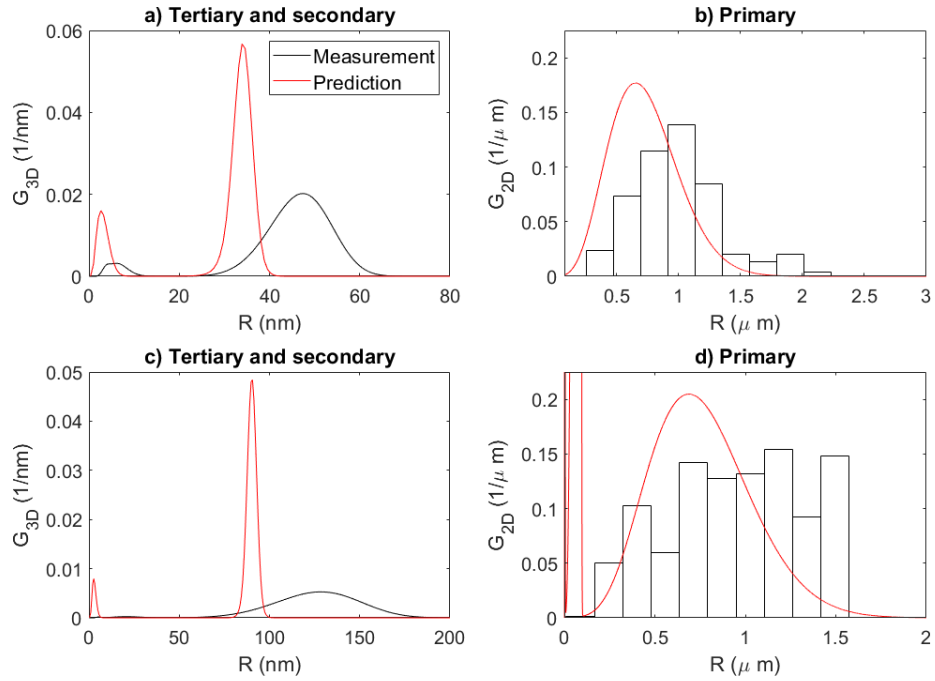


Figure 14: A comparison of the predicted and measured PRDs for sub-solvus SST with Figures a) and b) showing the results for an air cool and Figures c) and d) showing the results for the furnace cool. Figures a) and c) compare predictions with data obtained from analysis of TEM data, considering the 3D size of the precipitates.

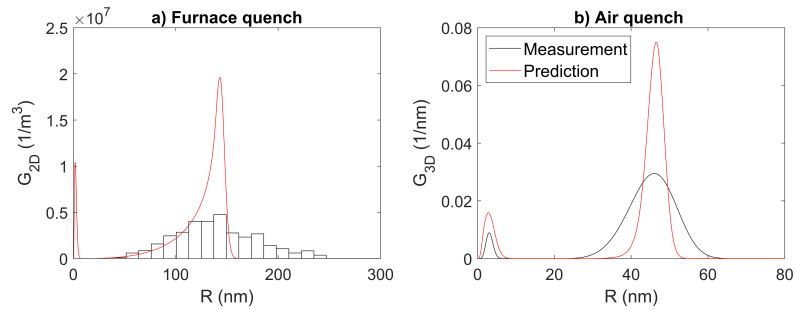


Figure 15: A comparison of experimental data with the predicted dispersions considering a super-solvus SST with either a) an air cool, or b) a furnace cool. Figure a) compares the 3D size of the precipitates, utilising data obtained from TEM micrographs, whilst Figure b) calculates the 2D PRD from the predicted dispersion for comparison with data obtained from SEM micrographs.

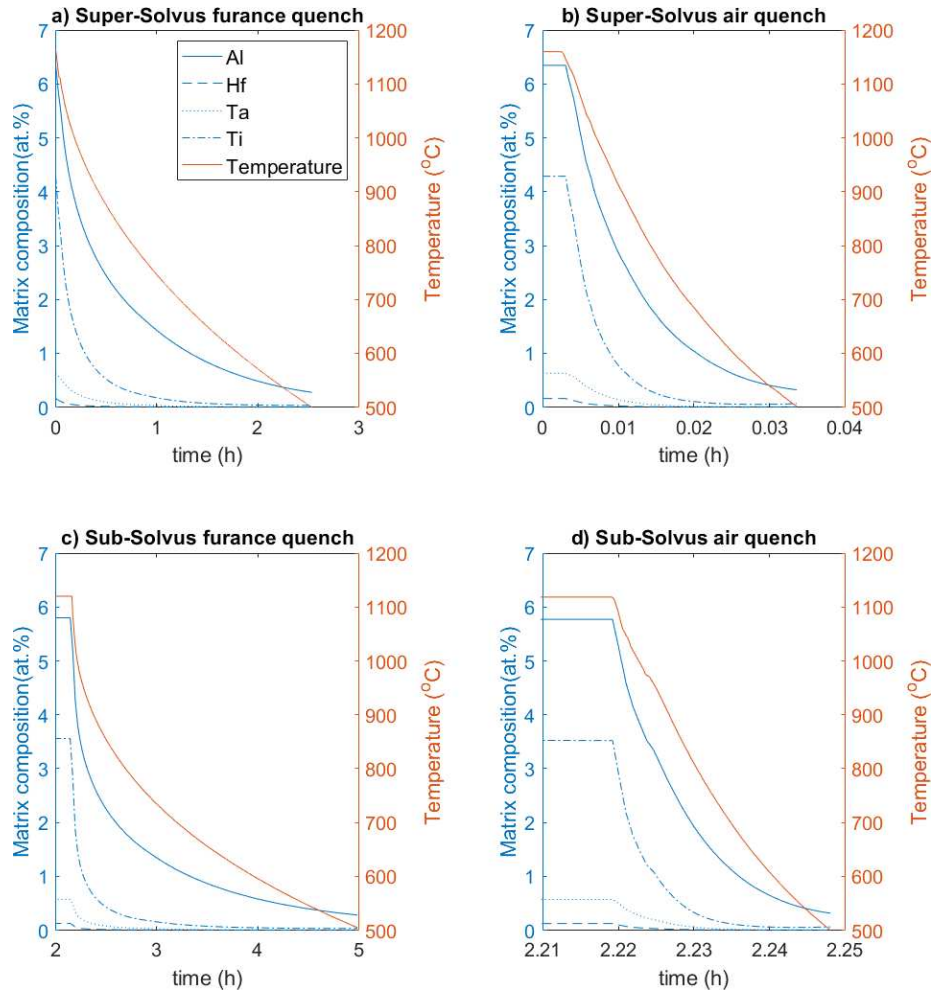


Figure 16: The predicted evolution of the matrix composition during SST and quench from a super-solvus temperature and a sub-solvus temperature. Figures a) and b) describe the SST followed by a furnace quench and air quench, respectively. Figures c) and d) describe a sub-solvus SST followed by a furnace quench and air quench, respectively.

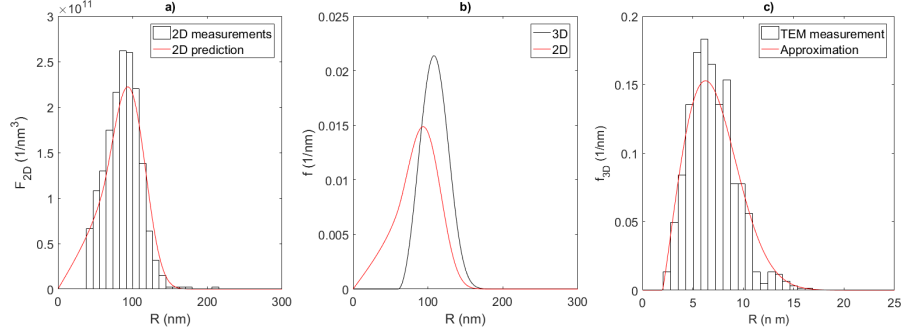


Figure 17: The calculation of the initial PRD descriptive of coarse-grain RR1000 for use in mean-field modelling. Figure a) compares the PRD measured from SEM micrographs with the approximated dispersion. Figure b) shows the approximated 3D distribution and the associated 2D distribution of particle cross sections. Figure c) shows the PRD used to capture the 3D size of the tertiary particles.

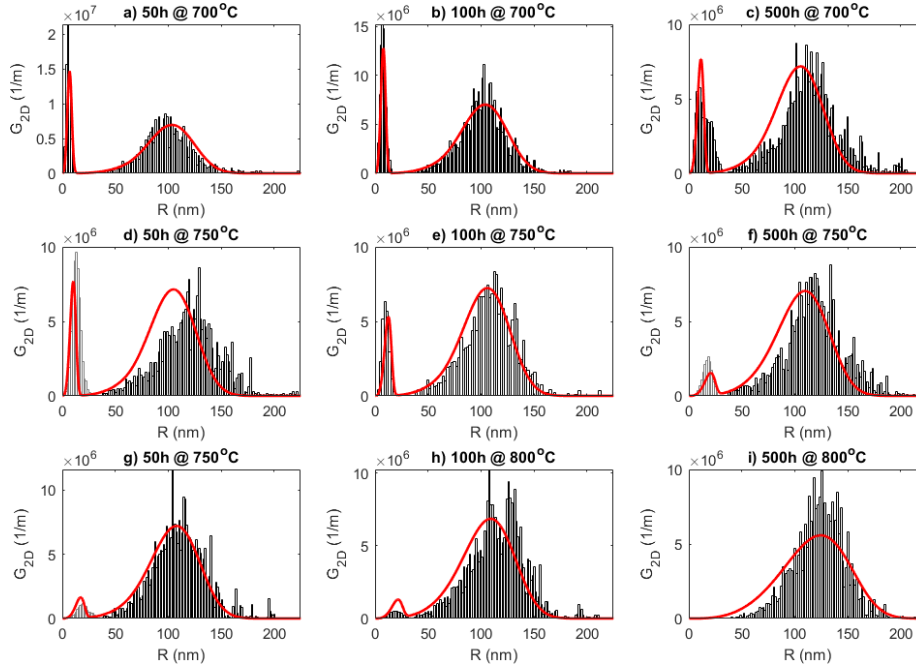


Figure 18: A comparison of the measured and predicted PRDs during isothermal aging of coarse-grain RR1000. The tertiary distributions shown in grey originate from SEM micrographs.

the tertiary precipitates, and one without. These are denoted by "Anderson *et al.* (2020)" and "Anderson *et al.* (2018)", respectively. During coarsening, the mean-field precipitation model predicts minimal solute super saturation in the matrix. As a result, the value of  $\chi_i$  in Equation 37 approaches unity, and the model predicts similar behaviour to that presented by Anderson *et al.* [14] during coarsening. Figure 19 a), b), and c) show the coarsening kinetics at 700°C, 750°C and 800°C, respectively. It can be seen that without the phenomenological model, the volume fraction of tertiaries is predicted to decrease from the onset of aging, and does not capture the stability of the tertiary precipitates observed at 700°C. The measurements suggest an increase in tertiary volume fraction during aging at 700°C. The model does not capture this behaviour, with the volume fraction of particles rapidly growing to reach the equilibrium volume fraction. Figure 19 c) shows two drops in the volume fraction of tertiary when examining the predictions of the model presented in this work. This behaviour is caused by a shift from coarsening to dissolution kinetics of the tertiary particles as  $\eta$  approaches zero.

It is possible that the precipitate dispersion is still within the regime of growth during the aging heat treatments examined in this work. Precipitate forming solute may be trapped within the depletion zones that develop during the quench. During aging, the trapped solute would slowly diffuse to the surrounding particles, allowing the tertiary to grow rather than dissolve.

Other explanations that may contribute to the stability of the tertiary particles include local spatial variations in both composition and lattice distortion. It is possible to model the evolution of the precipitate compositions of the particle populations as they nucleate and grow in a mean-field formulation. The compositions of the particle populations vary due to the different conditions at which the particles nucleate. The compositions of the precipitates evolve towards a dynamic equilibrium, however the larger particles take longer to change composition resulting in the differences in composition being locked in. The tertiary precipitates have a composition closer to the dynamic equilibrium, contributing to their stability. Svoboda *et al.*'s [10] model framework includes the ability

to capture the evolution of the precipitate composition. A key detail such a model lacks is the difference in matrix composition neighbouring the different precipitate populations and how the matrix composition evolves with time. The matrix composition would not stay static, and the depletion zones homogenize during exposure to elevated temperature. The simplest model that captures this behaviour are the 1D phase field models [described by Kitashima \*et al.\* \[35\]](#) and Fleck *et al.* [36]. This approach offers the benefits of capturing coalescence events, the formation and homogenization of the depletion zone, including the impact of the misfit strain energy upon particle the growth rate, and [capturing the interacting diffusion fields explicitly](#). A 1D description still requires significant computation to determine the spatial variation of chemical potentials with sufficient resolution to capture the diffusion profiles of a statistically representative number of particles.

The increase in misfit strain interaction energy between secondary precipitates could slow their growth, allowing for the continued growth and stability of the tertiary precipitates. Thornton *et al.* [37] coined the expression "inverse coarsening" to describe the scenario where a smaller precipitate grows at the expense of a larger precipitate due to energy minimisation considering contributions from both interfacial energy and elastic misfit energy. The secondary particles may grow into cuboidal geometry rather than continuing to grow isotopically, reducing their growth rate compared to the tertiary precipitates.

Coalescence of tertiary precipitates would allow their size to increase quickly, prolonging the time needed to dissolve the precipitates when they eventually come into direct competition with secondary particles for solute.

Another approach is to determine precipitate kinetics as a direct function of the particle's immediate environment through modelling the spatial arrangement of the precipitates [38, 39]. The clustered tertiary precipitates would compete with their immediate neighbours rather than the secondary particles, until the secondary particles grow to directly compete with the tertiary particles.

A phenomenological  $\mathcal{C}$  parameter was introduced to reduce the kinetics of isolated tertiary particles in Equation 43. The need for this reduction in kinetics

may arise from a number of possibilities. Composition differences are known to develop between the different populations of  $\gamma'$  in RR1000 [4]. It is likely that the fast diffusing  $\gamma'$  forming solutes are quickly absorbed by secondary precipitates. The tertiary  $\gamma'$  are likely to form from the slower diffusing elements remaining in the matrix, which may contribute to their slower growth kinetics. Ardell and Ozolins [40] proposed that during certain regimes, the growth rate of a particle may be limited by the rate at which solute is absorbed through the particle/matrix interface opposed to the rate at which solute diffuses through the matrix. This may explain or contribute to the need to reduce the tertiary precipitate growth rate by the coefficient  $\mathcal{C}$ . Plotnikov *et al.* [41] have observed the reduction of the  $\gamma/\gamma'$  interface during coarsening of  $\gamma'$  in binary Ni-Al alloys. This would suggest that the tertiary precipitates have a larger interface, with slower kinetics following the Trans-Interface diffusion-controlled (TIDC) model [40].

It is likely that all the mechanisms discussed contribute to the relative stability of the tertiary particles.

## 6.2. Pseudo-binary descriptions

This work has utilised commercial thermodynamic and mobility databases to determine precipitate kinetics, however a pseudo-binary approximation may be utilised to determine both the chemical driving force and mobility parameters [42]. The chemical driving force can be approximated by [43]

$$\Delta G_c = \frac{(C_\gamma - C_{\gamma'}) R_g T \ln(C_\gamma/C_m)}{(1 - C_\gamma) T_f} \quad (47)$$

$$T_f = 1 + \frac{\partial v}{\partial C_\gamma}$$

where  $C_\gamma$  and  $C_{\gamma'}$  are the summation of  $\gamma'$  forming equilibrium compositions within the matrix and particles, respectively. The term  $v$  is the activity and  $T_f$  is the thermodynamic factor.  $C_m$  is the pseudo-binary solute fraction of particle forming species within the matrix, which is calculated from

$$C_m = \frac{C_b - \phi C'_\gamma}{1 - \phi} \quad (48)$$

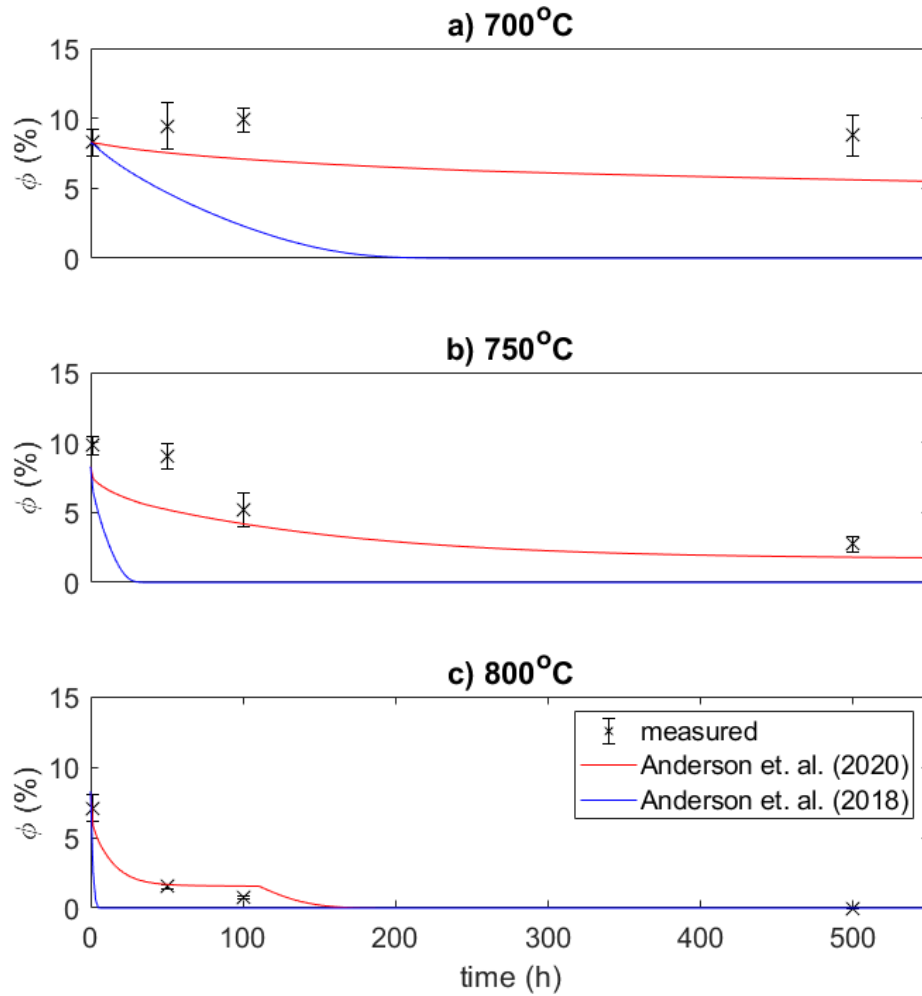


Figure 19: A comparison of the predicted and measured evolution of the volume fraction of tertiary precipitates considering kinetics at a) 700°C, b) 750°C, and c) 800°C. The predictions using the proposed model are compared against those without the phenomenological treatment of the isolated tertiary precipitates.

$C_b$  is the bulk composition of particle forming species. The binary form of the  $\theta$  expression appearing in both the particle grow rate and atomic attachment rate (Equations 18 and 36), including the super-saturation term is given below

$$\theta = \chi_m C_m D_v V_m \quad (49)$$

where  $\chi_m$  is the diffusion distance term considering the pseudo-binary matrix composition and  $D_v$  is the rate limiting diffusivity. The equilibrium pseudo binary composition has been approximated by summing the  $\gamma'$  formers (Al, Hf, Ta, and Ti in RR1000) from equilibrium calculations for  $\gamma'$  and  $\gamma$  in RR1000 using the thermodynamic database TTNi8 shown in Figure 12 b). The chemical driving force calculated from Equation 16 and 47 are compared in Figure 20 a), b) and c) for different volume fractions of  $\gamma'$  up to the equilibrium volume fraction, and for three temperatures. The temperatures assessed have been normalised by the solvus temperature  $T_s$ . The thermodynamic factor was set to  $T_f = 1$  for the pseudo-binary chemical driving force. At high temperature the results are similar as seen in Figure 20 c), however the trend in behaviour deviates significantly at lower temperature, as observed in Figure 20 a). The multi-component description of the chemical driving force is capturing interaction effects between the alloying elements which is missing in the pseudo-binary approximation. The impact of these interactions reduce with an increase in temperature [44]. A more detailed approximation of the thermodynamic factor shown in Equation 47 may resolve this deficiency.

The model has been implemented using the pseudo-binary approximations for the chemical driving force and the mobility term shown in Equations 47 and 49). The effective diffusivity and interfacial energy have been calibrated to capture the size of the secondary precipitates. Figure 20 d) and e) compares the predicted precipitation dispersions with measurements using both the multi-component formulation, and the pseudo-binary formulation, considering the air cooled and furnace cooled super-solvus SST conditions. The pseudo-binary approximation predicts larger secondary precipitates in the furnace cooled condition shown in Figure 20 e), however is still within the data. Differences are

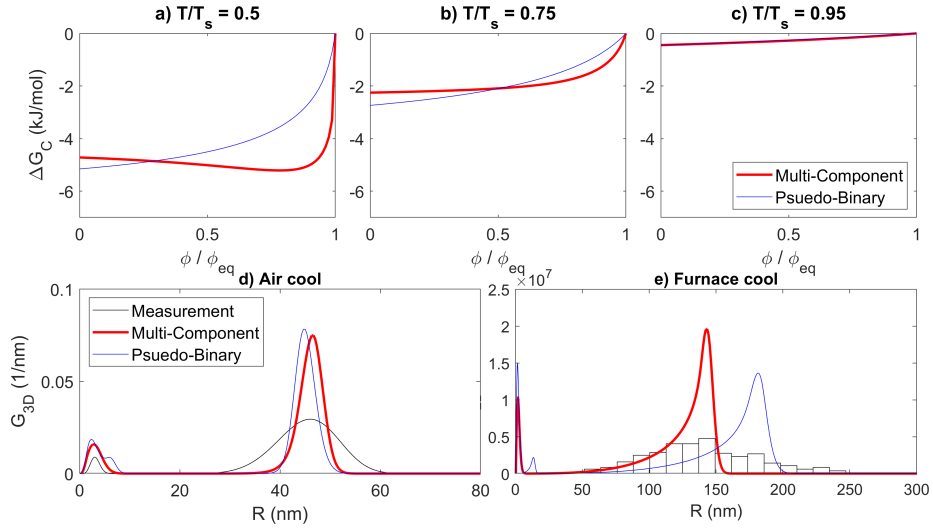


Figure 20: a), b) and c) The chemical driving force for the  $\gamma \rightarrow \gamma'$  phase transformation comparing the multi-component and pseudo-binary approximations shown in Equations 16 and 47, respectively. The x-axis shows the volume fraction of particles normalised by the equilibrium volume fraction. The temperatures considered are shown as a fraction of the solvus temperature of  $\gamma'$  in  $\gamma$  ( $T_s \sim 1150^\circ\text{C}$ ). d) A comparison of the measured and predicted dispersions considering the furnace cooled super-solvus SST using the multi-component and pseudo-binary formulations respectively. e) A comparison of the measured and predicted dispersions considering the air-cooled super-solvus SST using the multi-component and pseudo-binary formulations respectively.

also observed when comparing the tertiary precipitates, with the pseudo-binary approximation predicting larger tertiary particles in the case of the air cooled specimen, and an additional population of tertiary precipitates for the furnace cooled condition. It can be seen that the multi-component formulation of the chemical driving force and diffusivities using the TTNi8 and MOBNi1 databases is successful in capturing effects arising from strong coupling between thermodynamic and kinetic effects which are missing from the pseudo-binary approximation considering  $\gamma'$  kinetics in RR1000.

## 7. Conclusions

- The precipitation kinetics of  $\gamma'$  in the Ni based superalloy RR1000 has been characterised, examining conditions relevant to alloy processing and service conditions in aerospace applications.
- A framework is presented for the collation of data obtained from SEM and TEM for comparison with mean-field predictions. This includes the development of a new method for estimating the size and volume fraction of precipitates from TEM micrographs and an analytical solution for the 3D $\rightarrow$ 2D conversion of the PRD function.
- Measurements of the tertiary precipitates during isothermal aging of as-heat treated course grain RR1000 show that these particles coarsen during conditions where mean-field precipitation models suggests that they should dissolve.
- A phenomenological mean-field model has been developed that captures the observed coarsening behaviour of the tertiary precipitates. Continuity equations and particle growth rates are presented for each type of precipitate, and are linked using appropriate source and sink terms. An Avrami parameter describes the evolution of the fraction of isolated tertiary precipitates. During the regime of coarsening, the critical particle radius of the isolated tertiary particles is determined through the conservation of solute within the isolated tertiary particle population.

### Appendix: Determination of the critical particle radius of a coarsening dispersion

During coarsening of a precipitate dispersion, solute within the particle phase is conserved, and the volume fraction remains constant. The change in volume fraction of the dispersion is given by

$$\frac{d\phi}{dt} = \frac{4\pi}{3} \frac{d}{dt} \int_0^\infty \mathcal{F} R^3 dR \quad (50)$$

Performing the derivative leads to

$$\frac{d\phi}{dt} = \frac{4\pi}{3} \int_0^\infty \left( \frac{d\mathcal{F}}{dt} R^3 dR + 3\mathcal{F} R^2 V dR + \mathcal{F} R^3 \frac{d}{dR}(dR) \right) \quad (51)$$

where  $V$  is the particle growth rate. We can make use of the following relationship

$$\frac{d}{dR}(dR) = \frac{\partial V}{\partial R} dR \quad (52)$$

Substituting Equation 52 into Equation 51 gives

$$\frac{d\phi}{dt} = \frac{4\pi}{3} \int_0^\infty \left( \frac{d\mathcal{F}}{dt} R^3 dR + 3\mathcal{F} R^2 V dR + \mathcal{F} R^3 \frac{\partial V}{\partial R} dR \right) \quad (53)$$

The material derivative of  $\mathcal{F}$  is given by

$$\frac{d\mathcal{F}}{dt} = \frac{\partial \mathcal{F}}{\partial t} + V \frac{\partial \mathcal{F}}{\partial R} \quad (54)$$

Equation 54 may be substituted into Equation 53 and then by grouping terms we arrive at

$$\frac{d\phi}{dt} = \frac{4\pi}{3} \int_0^\infty \left\{ \left( \frac{\partial \mathcal{F}}{\partial t} + V \frac{\partial \mathcal{F}}{\partial R} + \mathcal{F} \frac{\partial V}{\partial R} \right) R^3 + 3\mathcal{F} R^2 V \right\} dR \quad (55)$$

This may be simplified using the chain rule

$$\frac{d\phi}{dt} = \frac{4\pi}{3} \int_0^\infty \left\{ \left( \frac{\partial \mathcal{F}}{\partial t} + \frac{\partial}{\partial R}(\mathcal{F}V) \right) R^3 + 3\mathcal{F} R^2 V \right\} dR \quad (56)$$

The continuity equation governing precipitate kinetics may be defined by

$$\frac{\partial \mathcal{F}}{\partial t} + \frac{\partial}{\partial R}(\mathcal{F}V) = \mathcal{I} \quad (57)$$

where the term  $\mathcal{I}$  groups together source and sink terms ( $\dot{\mathcal{F}}^+(R, t)$  and  $\dot{\mathcal{F}}^-(R, t)$  in Equation 10). Substituting Equation 57 into Equation 56 and then separating variables gives

$$\frac{d\phi}{dt} = \frac{4\pi}{3} \int_0^\infty \mathcal{I} R^3 dR + 4\pi \int_0^\infty \mathcal{F} R^2 V dR \quad (58)$$

The first integral shows how the volume fraction changes as a response to any source and sink terms, such as nucleation. The second integral is the change in volume fraction as a result of the particle growth rate,  $V$ . During coarsening,  $\mathcal{I} = 0$  and  $\frac{d\phi}{dt} = 0$  simplifying Equation 58 to

$$\int_0^{\infty} \mathcal{F} R^2 V dR = 0 \quad (59)$$

An expression for the critical particle radius can be obtained by inserted the generic form for the particle growth rate shown in Equation 11 into Equation 59, and rearranging for  $R_c$

$$R_c = \frac{\int_0^{\infty} \mathcal{F} R z dR}{\int_0^{\infty} \mathcal{F} z dR} \quad (60)$$

### Acknowledgements

We thank the Aerospace Technology Institute (ATI) for funding this work through the Manufacturing Portfolio programme (project number 113084). The authors would like to show their gratitude to the Rolls-Royce process modelling team for technical support. A special thanks to Professor Cathie Rae and Dr Hon Tong Pang for their assistance in the preparation of the TEM specimens. The authors express their appreciation to the reviewers of the manuscript who made strong contributions to improving this work. The computations described in this paper were performed using the University of Birmingham's BlueBEAR HPC service, which provides a High Performance Computing service to the University's research community. See <http://www.birmingham.ac.uk/bear> for more details.

### References

- [1] J. Christian, The theory of transformations in metals and alloys, Pergamon, Oxford, 2002, pp. 422 – 479.

- [2] M. Doi, Coarsening behaviour of coherent precipitates in elastically constrained systems, *Mater. Trans., JIM* 33 (7) (1992) 637–649.
- [3] M. Thompson, C. Su, P. Voorhees, The equilibrium shape of a misfitting precipitate, *Acta Metall.* 42 (6) (1994) 2107–2122.
- [4] Y. Q. Chen, T. J. A. Slater, E. A. Lewis, E. M. Francis, M. G. Burke, M. Preuss, S. J. Haigh, Measurement of size-dependent composition variations for gamma prime ( $\gamma'$ ) precipitates in an advanced nickel-based superalloy, *Ultramicroscopy* 144 (2014) 1–8.
- [5] I. M. Lifshitz and V. V. Slyozov, The kinetics of precipitation from supersaturated solid solutions, *J. Phys. Chem. Solids* 19 (1961) 35–50.
- [6] C. Z. Wagner, Theorie der alterung von niederschlagen durch umlonsen (Ostwald-reifung), *Z. Elektrochem* 65 (1961) 581–591.
- [7] M. K. Chen and P. W. Voorhees, The dynamics of transient Ostwald Ripening, *Modell. Simul. Mater. Sci. Eng.* (1993) 1, 591-612.
- [8] Q. Chen, J. Jeppsson, J. Agren, Analytical treatment of diffusion during precipitate growth in multicomponent systems, *Acta. Mater.* 56 (8) (2008) 1890–1896.
- [9] T. Philippe and P. H. Voorhees, Ostwald ripening in multicomponent alloys, *Acta. Mater.* 61 (11) (2013) 4239–4244.
- [10] J. Svoboda, F. D. Fischer, P. Fratzl, E. Kozeschnik, Modelling of kinetics in multi-component multi-phase systems with spherical precipitates - I: Theory, *Mater. Sci. Eng. A Struct. Mater.* 385 (1-2) (2004) 166–174.
- [11] T.P. Gabb, D. G. Backman, D. Y. Wei, D. P. Mourer, D. Furrer, A. Garg, D. L. Ellis,  $\gamma'$  formation in a nickel-base disc superalloy, in: Pollock, TM and Kissinger, RD and Bowman, RR and Green, KA and McLean, M and Olson, SL and Schirra, JJ (Ed.), *Superalloys 2000*, TMS Seven Springs Int Symp Comm; TMS High Temp Alloys Comm; ASM Int, 2000, pp. 405–414.

- [12] H. Jou, P. Voorhees, G. Olson, Computer simulations for the prediction of microstructure/property variation in aeroturbine disks, in: Green, KA and Pollock, TM and Harada, H and Howson, TE and Reed, RC and Schirra, JJ and Walston, S (Ed.), *Superalloys 2004*, TMS Seven Springs Int Symp Comm; TMS High Temp Alloys Comm; ASM Int, 2004, pp. 877–886.
- [13] M. J. Anderson, A. Rowe, J. Wells, H. C. Basoalto, Application of a multi-component mean field model to the coarsening behaviour of a nickel-based superalloy, *Acta Mater.* 114 (1) (2016) 80–96.
- [14] M.J. Anderson, C. Panwisawas, Y. Sovani, R.P. Turner, J.W. Brooks, H.C. Basoalto, Mean-field modelling of the intermetallic precipitate phases during heat treatment and additive manufacture of Inconel 718. *Acta mater.* (2018), **156**, 432-445.
- [15] M.J. Anderson, J. Benson, J.W. Brooks, B. Saunders, H.C. Basoalto, Predicting Precipitation Kinetics During the Annealing of Additive Manufactured Inconel 625 Components. *Integr. Mater. Manuf. Innov.* (2019) 8 (2), 154-166.
- [16] S.L. Semiatin, M.C. Levkulich, J.S. Tiley, An Investigation of Tertiary  $\gamma'$  Precipitation in a Powder-Metallurgy,  $\gamma$ - $\gamma'$  Nickel-Base Superalloy Metall. *Mater. Trans. A* (2019) 50A (11), 5281-5296.
- [17] M. Li, J. Coakley, D. Isheim, F. Tian. B. Shollock, Nickel base superalloy,  $\gamma/\gamma'$  composition, Atom probe tomography, Particle size distribution, Nucleation and growth, *J. Alloy Compd.* (732) (2018) 765–776.
- [18] R. Radis, M. Schaffer, M. Albu, G. Kothleitner, P. Pölt, E. Kozeschnik, Multimodal, Nickel alloy, Precipitation, Nucleation and growth, Phase transformation kinetics, *Acta Mater.* 57 (19) (2009) 5739 - 5747.
- [19] A. Finel, Y. Le Bouar, A. Gaubert, O. Salman, Phase field methods: Microstructures, mechanical properties and complexity. *C. R. Phys.* (2010,) 11, 245-256.

- [20] R. Duddu, D.L. Chopp, P. Voorhees, B Moran, Diffusional evolution of precipitates in elastic media using the extended finite element and the level set methods. *J. Comput. Phys.* (2011,) 230 (4), 1249-1264.
- [21] E. J. Payton, P. J. Phillips, M. J. Mills, Semi-automated characterization of the  $\gamma'$  phase in Ni-based superalloys via high-resolution backscatter imaging, *Mater. Sci. Eng., A* 527 (10-11) (2010) 2684–2692.
- [22] C. T Rueden, J. Schindelin, M. C Hiner, B. E DeZonia, A. E Walter, E. T Arena, K. W Eliceiri, ImageJ2: Imagej for the next generation of scientific image data, *BMC Bioinformatics* 18 (1) (2017) 529.
- [23] Matlab image processing toolbox (2016).
- [24] A.R.C Gerlt, R.S Picard, A.E Saurber, A.K Criner, S.L Semiatin, E.J Payton, A Transfer Function for Relating Mean 2D Cross-Section Measurements to Mean 3D Particle Sizes *Metall. Mater. Trans. A* 49A (10), (.2019)4424-4428.
- [25] A. N. Diogenes, L.O.E. dos Santos, C.P Fernandes, Particle size distribution correction method using a simulated annealing technique, *Therm Eng+* . 10 (2011) 38–43.
- [26] B. Sonderegger, Modifications of stereological correction methods for precipitate parameters using transmission microscopy, *Ultramicroscopy* 106 (10) (2006) 941 – 950.
- [27] P. M. Kelly, A. Jostsons, R. G. Blake, J. G. Napier, The determination of foil thickness by scanning transmission electron microscopy, *physica status solidi (a)* 31 (2) (1975) 771–780.
- [28] H. C. Basoalto, The 3D→2D conversion of particle radii distribution functions, personal communication (2017)
- [29] J. A. Marqusee, J. Ross, Theory of Ostwald Ripening - Competitive growth and its dependence on volume fraction, *J. Chem. Phys.* 80 (1) (1984) 563–543.

- [30] E. Clouet, Modeling of nucleation processes, ASM Handbook, 2010.
- [31] H. B. Aaron, D. Fainstein, G. Kotler, Diffusion-Limited Phase Transformations: A Comparison and Critical Evaluation of the Mathematical Approximations, *J. Appl. Phys.* 41 (11) (1970) 4404–4410.
- [32] A.R.P. Singh, S. Nag, J. Y. Hwang, G. B. Viswanathan, J. Tiley, R. Srinivasan, H. L. Fraser, R. Banerjee, Influence of cooling rate on the development of multiple generations of  $\gamma'$  precipitates in a commercial nickel base superalloy, *Mater. Charact.* 62 (9) (2011) 878–886.
- [33] J. Andersson, T. Helander, L. Höglund, P.F. Shi, B. Sundman, THERMOCALC & DICTRA, computational tools for materials science, *CALPHAD* 26 (2) (2002) 273–312.
- [34] H. S. Kitaguchi, I. P. Jones, Y. Chiu, R. Ding, M. C. Hardy, P. Bowen, Mesoscopic quantitative chemical analyses using STEM-EDX in current and next generation polycrystalline Ni-based superalloys, *Ultramicroscopy* 204 (2019) 55 - 72.
- [35] T. Kitashima, D. Ping, W. Jincheng, H. Harada, Phase-field modeling of  $\gamma'$  precipitation in multi-component Ni-base superalloys (Ed.), *Superalloys 2008*, 11th International Symposium on Superalloys; TMS High Temp Alloys Comm; ASM Int, 2008, pp. 819–827.
- [36] M. Fleck, F. Schleifer, M. Holzinger, U. Glatzel, Phase-Field Modeling of Precipitation Growth and Ripening During Industrial Heat Treatments in Ni-Base Superalloys, *Metall. Mater. Trans. A* 49 (9) (2018) 4146–4157.
- [37] K. Thornton, N. Akaiwa, P. Voorhees, Large-scale simulations of Ostwald ripening in elastically stressed solids: I. Development of microstructure, *Acta Mater.* 52 (5) (2004) 1353–1364.
- [38] P. Voorhees, M. Glicksman, Solution to the multi-particle diffusion problem with applications to Ostwald Ripening. 1. Theory, *Acta. Metall. Mater.* 32 (11) (1984) 2001–2011.

- [39] K. Wang, M. Glicksman, K. Rajan, Length scales in phase coarsening: Theory, simulation, and experiment, *Comput. Mater. Sci.* 34 (3) (2005) 235–253.
- [40] A.J. Ardell, V. Ozolins, Trans-interface diffusion-controlled coarsening, *Nat. Mater.* 4 (4) (2005) 309–316.
- [41] E.Y. Plotnikov, Z. Mao, Zugang and R.D. Noebe, D.N Seidman, Temporal evolution of the  $\gamma(\text{fcc})\gamma'(\text{L1}(2))$  interfacial width in binary Ni-Al alloys, *Scripta Mater.* 70 (2014) 51–54.
- [42] S.L Semiatin, S.L Kim, F. Zhang, J.S Tiley, An Investigation of High-Temperature Precipitation in Powder-Metallurgy,  $\gamma/\gamma'$  Nickel-Base Superalloys *Metall. Mater. Trans. A* 46 (4)(2015) 1715-1730.
- [43] R.D Doherty: in *Physical Metallurgy*, R.W. Cahn, P. Haasen, North-Holland, Amsterdam, (1996), ch.15.
- [44] D.A. Porter, K.E. Easterling: *Phase Transformations in Metals and Alloys*, Van Nostrand Reinhold Co Ltd., Wokingham, Berkshire, England (1984)